

Charge and heat transport of doped 8-*Pmmn* borophene with and without relaxation time approximation

B. D. Napitu*

Magnetic and Photonic Research Group, Institut Teknologi Bandung, Ganesha 10, Bandung 40132, Indonesia

(Received 16 January 2023; revised 3 April 2023; accepted 12 April 2023; published 27 April 2023)

Charge and heat transport of monolayer borophene are investigated by means of Boltzmann's transport equation, which is solved self-consistently and analyzed with the relaxation time approximation (RTA). To simulate a realistic experimental condition, a borophene monolayer is first considered to be affected by two types of randomly distributed impurity. Charge transport near the Dirac neutrality point and highly-doped regime changes according to the orientation of measurement, which reflects the anisotropy of the Dirac cone. Characteristic of electron at large doping follows the typical free electron gas but then decays onto interacting like ensemble at low doping signalled by an increase of resistivity around zero doping and a violation of Wiedemann-Franz's law. When acoustic phonon is accounted for, charge transport is found to be sensitive to the magnitude of electron-phonon interaction yielding further enhancement of resistivity at low and large doping. A resistivity consists of T^4 power law at low temperature, which evolves onto linear T at high temperature. A similar trend is also observed when borophene is deposited on top of polar substrate, which manifests itself in the resistivity and mobility. Depending on the dielectric constant of the substrate, remote phonon scattering is shown to substantially affect transport at room temperature in a way that ultrahigh mobility at the order of 10^6 cm²/Vs falls down to the order of 10^4 cm²/Vs. In contrast to charge transport, heat quantities such as thermopower, figure of merit do not provide any signature of anisotropy of low-energy dispersion and deviate from the Mott's formula. The impact of impurity or perturbation by lattice vibration could, however, be recognized upon varying temperature and charge density carrier. An interesting signature of electron-phonon interaction is shown by phonon drag effect, which not only varies with temperature according to T^3 but also depends on the orientation. It is argued that this unique trait might be a useful tool for the search of phonon drag effect in borophene, which has been proven to be difficult in other two-dimensional systems. The analysis is further elaborated with a survey on the electron cooling mechanism involving acoustic and optical phonon. At low temperature, power loss indicates that energy exchange between hot carrier and its environment depends on the carrier density, tilted velocity and dielectric constant. The use of polar substrate is shown to provide additional channel for relaxation of energy and momentum of hot electrons facilitating a faster cooling at high temperature.

DOI: [10.1103/PhysRevB.107.155435](https://doi.org/10.1103/PhysRevB.107.155435)

I. INTRODUCTION

One of the most interesting alternatives to graphene synthesized recently is borophene β_{12} constituting of boron (B) atoms on the Ag(111) substrate [1–3]. It has a metallic characteristic that arises from a novel atomic configuration on two-dimensional plane and it consists of an out-of-plane buckling sheets [4]. Following an *ab initio* calculations, two-dimensional boron polymorph manifests itself in a number of stable crystal structures classified as α and γ phase with 2-*Pmmn* and 8-*Pmmn* sheet space symmetry [5–9]. The emergence of rich allotropes, which is furnished by a distinctive symmetry has been related to a deficiency of electron in boron atom. It also offers an advantage in its own right, namely, that it allows for a complex framework of σ and π bonds. Under certain conditions, i.e., by control of pressure or temperature, it is possible to shift covalent bonds onto ionic bonds [10].

Experimental realization of monolayer borophene beyond β_{12} phase has been, however, quite challenging. One main obstacle has been its low stability even beyond room temperature 450°–550 °C. Another challenge is the realization of a freestanding layer, which has been suggested to harbor many intriguing properties. It is currently not clear whether a freestanding layer could be realized for all allotropes of borophene, since, theoretically such state is shown to be rather unlikely due to the presence of imaginary energy in the phononic dispersion [11,12]. Recently, however, there has been an experimental report on the possibility of synthesis of a freestanding borophene, i.e., β_{12} , which is achieved by liquid phase exfoliation [13].

Being an adjacent element to the carbon atom in the periodic table, one naturally expects that borophene might share a number of outstanding attributes of graphene. It is, however, difficult to compare both systems since for β_{12} to appear, it requires a support of substrate such as Ag(111). This is in contrast to graphene in which a freestanding monolayer is stable and synthesizable, i.e., could be derived directly from a bulk in a straightforward experimental procedure. We recall

*bdnapitu@itb.ac.id

that a monolayer graphene with an almost flat honeycomb lattice is known to exhibit an ultrahigh mobility up to $2 \times 10^5 \text{ cm}^2 \text{ V}^{-1} \text{ s}^{-1}$ and inherently large thermal conductivity, which is in the range of 2600 to 5300 W/mK near 350 K [14–16].

The outstanding transport properties of graphene, which is known to exceed that of Si, however, deteriorates once the substrate is introduced. This step is known to help reduce charge inhomogeneity and is essential to increase the functionality of graphene, i.e., allowing for an integration with other systems. From a number of experiments we are aware that the use of SiO_2 leads to the decrease of charge mobility down to the order of 2000–17000 $\text{cm}^2 \text{ V}^{-1} \text{ s}^{-1}$ [17,18]. On the other hand when graphene is combined with boron nitride or on top of SiC, characteristic of transport improves in a way that mobility reaches up to 18100–27000 $\text{cm}^2 \text{ V}^{-1} \text{ s}^{-1}$ [19–21].

In retrospect with the borophene monolayer in which a substrate is somewhat a *conditio sine qua non*, a thorough understanding of the role of supporting material on electronic properties of borophene is thus of great importance. The effort toward this goal is, however, currently lacking and this is true not only to those already synthesized system such as β_{12} but also to a new class of borophene including those with $2\text{-}Pm\bar{m}n$ or $8\text{-}Pm\bar{m}n$ symmetry, which remain to be realized in the future experiment. As in the case of graphene, one naturally expects that borophene samples growing on different substrate might exhibit considerable variations of electronic and thermal properties. A judicious choice of substrate thus becomes crucial when one aspires for an optimal electronic properties of borophene. A successful endeavour along this line will be of service to both our scientific interest and the foreseeable future plan such as realization of interconverting heat and electricity, which holds a promise as an efficient energy source.

In an effort to resolve various issues on the role of substrate in the borophene monolayer, I present in this paper a study on transport properties of borophene with $8\text{-}Pm\bar{m}n$ symmetry under a weak external field or thermal gradient. This system has engendered a wide interest because of their unusual charge, thermal, and mechanical properties. Theoretical studies by means of density functional theories have indicated that pristine $8\text{-}Pm\bar{m}n$ borophene could resist an uniaxial stress up to 27.79 N/m along two lattice directions, owing to a large Young's modulus 398 GPa nm [11,22]. Under the same condition, model based calculations have also pointed out a number of novel phenomena such as anisotropic Friedel oscillation, undamped plasmon mode at high energies, Weiss oscillation in the magnetoconductivity, oblique Klein tunneling, direction-dependent optical conductivity [23–26]. Recent analysis on the interaction between monolayer borophene and high-frequency light suggests the possibility of quantized Hall effect and thermal rectification whereas a study on borophene based superconducting junction indicated the possibility of specular Andreev reflection [27–30].

Transport of $8\text{-}Pm\bar{m}n$ borophene on top of substrate has also been discussed recently in [31,32]. By means of Boltzmann transport, analysis is directed to identify the role of either impurity or acoustic phonon on charge and heat transport. While these studies have touched upon the role of

substrate, the analysis remains incomplete particularly since effect of scattering due to phonon or impurity has been considered partially and it is assumed to be disentangled. In a realistic system, scattering by impurity or phonon might coexist and this requires that they should be considered simultaneously in a theoretical description. In addition to this, a scattering on the Fermi surface has been treated differently using the relaxation time approximation (RTA) and self-consistent relation. It is not clear to what extent the relaxation time approximation could be employed in describing transport on borophene and how much it could agree with the iterative solution.

In order to provide a complete picture, the present study will be carried out on the basis of model description, which is combined with the Boltzmann's transport equation. It is aimed at elucidating various aspects that might affect charge and heat transport of borophene, which is deposited on top of substrate. This involves scattering by nonmagnetic impurities with different type of potential or influence of vibration by acoustic and optical phonon. On top of this I also elaborate the discussion by analyzing the impact of nonequilibrium phonon, which is responsible for the phonon-drag and energy relaxation mechanism. The former is expected to contribute onto thermopower whereas the latter tells the way hot carrier swaps energy with its surrounding environment. The results outlined in this paper will be useful when interpreting transport measurement of the $8\text{-}Pm\bar{m}n$ borophene, once sample could be synthesized.

In the next section I shall be outlining the model Hamiltonian, which is followed by a derivation of Boltzmann transport in terms of the mean-free path. I discuss its self-consistent implementation with and without electron-phonon coupling and then compare the results with the usual relaxation time approximation. A short discussion on the advantage or weakness of each approach in dealing with anisotropic band structure is also outlined. The discussion is then followed by an analytical analysis of phonon drag effect and the electron cooling mechanism. I conclude the paper by highlighting an important feature of charge and heat transport of the $8\text{-}Pm\bar{m}n$ borophene.

II. 2D TILTED DIRAC HAMILTONIAN

The single-particle effective model of pristine $8\text{-}Pm\bar{m}n$ borophene can be expressed as

$$H_0 = \eta \hbar (v_x k_x \sigma_x + v_y k_y \sigma_y + v_t k_y \sigma_0), \quad (1)$$

where η denotes ± 1 valleys [23,31]. $\sigma = (\sigma_0, \sigma_x, \sigma_y)$ being the Pauli matrices and $\mathbf{k} = (k_x, k_y)$ are the in-plane wave vectors in x and y direction. v_x and v_y are velocities of Dirac electrons moving along the x and y with a magnitude of $0.86 v_{F0}$ and $0.69 v_{F0}$, respectively, with $v_{F0} = 10^6$ m/s. v_t corresponds to the tilted velocity of the order of $0.32 v_{F0}$, which is responsible for a tilting of band structure.

The energy dispersion of the Hamiltonian (1) can be written as

$$\epsilon_{\mathbf{k},\pm} = \eta \hbar (v_t k_y \pm \sqrt{v_x^2 k_x^2 + v_y^2 k_y^2}), \quad (2)$$

which is shown in Fig. 1. It consists of the Dirac cone for electrons and holes, which touch each other at $\mathbf{k} = 0$ resembling that of graphene. Owing to the tilted velocity, the Dirac

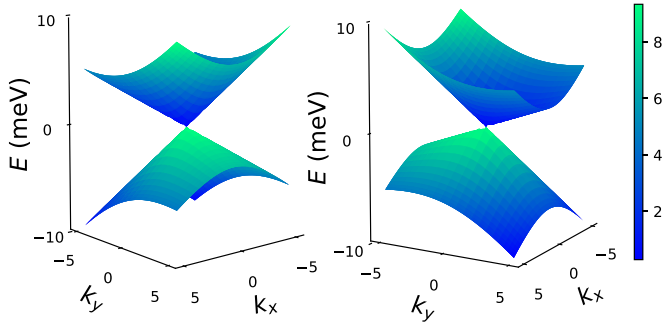


FIG. 1. The energy-band structure of two-dimensional borophene as a function of wave vectors k_x and k_y . The left and right panels correspond to valley indices $\eta = 1$ and $\eta = -1$, respectively. Here, the wave vectors have been renormalized by a factor of 10^7 .

cones are distorted to the negative k_y axis for $\eta = 1$ and to the positive axis for $\eta = -1$.

For the purpose of analytical derivation, it is useful to rewrite the Hamiltonian of Eq. (1) within the new variables p_x and p_y as follows:

$$\begin{aligned} p_x &= \sqrt{\frac{v_x}{v_y}} k_x, \\ p_y &= \sqrt{\frac{v_y}{v_x}} k_y, \end{aligned} \quad (3)$$

such that the Hamiltonian of Eq. (1) reduces onto

$$H = \eta \hbar v_F (p_x \sigma_x + p_y \sigma_y + v_0 p_y \sigma_0), \quad (4)$$

where $v_F = \sqrt{v_x v_y}$ and $v_0 = \frac{v_x}{v_y}$. With Eq. (4), the dispersion energy can be rewritten in the new variables and assumes the form of

$$\epsilon_{p\lambda} = \eta \hbar v_F (v_0 p_y + \lambda p), \quad (5)$$

with $p = \sqrt{p_x^2 + p_y^2}$ and $\lambda = \pm$. The knowledge of the dispersion relation Eq. (2) or Eq. (5) allows for the derivation of the density of states by using

$$D(\epsilon) = 2 \sum_{\lambda \mathbf{k}} \delta(\epsilon - \epsilon_{\mathbf{k}\lambda}),$$

which, after substitution, yields

$$D(\epsilon) = \frac{D_0}{\pi \hbar^2 v_F^2} |\epsilon|, \quad (6)$$

where

$$\begin{aligned} D_0 &= \int d\theta \frac{1}{\bar{z}^2(\theta)}, \\ \bar{z}(\theta) &= \frac{v_t}{v_F} \sin(\theta) + I_0(\theta), \end{aligned} \quad (7)$$

and

$$I_0(\theta) = \sqrt{\frac{v_x}{v_y} \cos^2(\theta) + \frac{v_y}{v_x} \sin^2(\theta)}. \quad (8)$$

By using the density of states, we can subsequently obtain the relation between the Fermi energy E_F and a given carrier density n as $E_F = \hbar v_F \sqrt{\frac{2\pi n}{D_0}}$.

Since the Fermi velocities of borophene are anisotropic, the corresponding Fermi surface is thus elliptical with eccentricity e determined by v_x and v_y in the form of $e = \frac{1}{v_x} \sqrt{v_x^2 - v_y^2}$. As a repercussion, the Fermi wave vector k_F does not depend only on the energy but also on the relative angle between momentum wave vectors denoted by $\tan(\theta) = k_y/k_x$. Explicitly, the Fermi wave vector k_F derived from Eq. (2) takes the form of

$$k_F = \frac{E_F}{\eta \hbar v_F \bar{z}(\theta)}. \quad (9)$$

As will be further discussed below, description of transport with momentum wave vectors that continuously changes along the Fermi surface demands a special treatment beyond that is usually employed for graphene.

In order to identify the amount of energy required to change a temperature, it may be preferable also to look at the electronic specific heat at fixed volume c_e , which can be calculated via $u = \int \epsilon f_0(\epsilon) D(\epsilon)$, for u being an internal energy and $f_0(\epsilon)$ denotes Fermi distribution function. By using Eq. (6), performing the integral, and taking derivative with respect to the temperature, i.e., $c_e = A \frac{du}{dT}$ one arrives at

$$c_e = \frac{9\zeta(3) D_0 k_B^3 T^2}{\pi (\hbar v_F)^2}, \quad (10)$$

where A being the area of the borophene sheet. Regardless of the prefactors, it is clear that the above expression resembles that of clean graphene consisting of power law behavior of T^2 .

III. TRANSPORT WITH ELASTIC SCATTERING

In the presence of charge impurities background or random vacancies, the low-energy Hamiltonian Eq. (1) is adjusted onto

$$H = H_0 + H_{\text{imp}}, \quad (11)$$

where $H_{\text{imp}} = \sum_i V(\mathbf{r} - \mathbf{R}_i) \sigma_0$ and $V(\mathbf{r} - \mathbf{R}_i)$ denotes the potential scattering of i th impurity at coordinate \mathbf{R}_i . For the sake of simplicity, it shall be assumed throughout that impurities are distributed on the two inequivalent borophene sublattice.

In order to describe the stochastic motion of quasiparticles, which underlies transport of charge or energy, we shall be solving Eq. (11) within the Boltzmann's transport equation. In this scheme, the flow of quasiparticles through solid is subsumed in the statistical distribution function $f_\lambda(\mathbf{k}, \mathbf{r}, t) \equiv f_{\mathbf{k},\lambda}$ with \mathbf{k} and \mathbf{r} being the two-dimensional electron wave and position vectors, respectively whereas t denotes time. When the system is subjected onto external static field, the distribution function follows the steady state Boltzmann equation, which can be written as

$$\mathbf{v}_{\mathbf{k}\lambda} \nabla_{\mathbf{r}} f_{\mathbf{k},\lambda} + \frac{\mathbf{F}}{\hbar} \nabla_{\mathbf{k}} f_{\mathbf{k},\lambda} = \left. \frac{\partial f_{\mathbf{k},\lambda}}{\partial t} \right|_c \quad (12)$$

where $\mathbf{v}_{\mathbf{k},\lambda} = \frac{1}{\hbar} \frac{\partial \epsilon_{\mathbf{k},\lambda}}{\partial \mathbf{k}}$ defines the velocity of electron on the $x-y$ plane whereas $\mathbf{F} = -e\mathbf{E}$ being the applied external electric field. The right-hand side of Eq. (12) is the rate of change of $f_{\mathbf{k},\lambda}$, which takes account of all possible collisions, such

as scattering events between electron and ionized impurities, static imperfections or absorption and emission of phonon. Explicitly, the collision term takes the form of

$$\left. \frac{\partial f_{\mathbf{k},\lambda}}{\partial t} \right|_c = \sum_{\mathbf{k}'\lambda'} [W_{\mathbf{k}'\lambda'\mathbf{k}\lambda} f_{\mathbf{k}',\lambda'} (1 - f_{\mathbf{k},\lambda}) - W_{\mathbf{k}\lambda\mathbf{k}'\lambda'} f_{\mathbf{k},\lambda} (1 - f_{\mathbf{k}',\lambda'})], \quad (13)$$

which under the principle of detailed balance and elastic scattering condition may be simplified onto

$$\left. \frac{\partial f_{\mathbf{k},\lambda}}{\partial t} \right|_c = \sum_{\mathbf{k}'\lambda'} W_{\mathbf{k}'\lambda'\mathbf{k}\lambda} [f_{\mathbf{k}',\lambda'} - f_{\mathbf{k},\lambda}], \quad (14)$$

with $W_{\mathbf{k}',\mathbf{k}}$ representing scattering probability from \mathbf{k} onto \mathbf{k}' state. Assuming an impurity potential V , which only amounts to inducing weak disturbances, the scattering probability shall be determined within the Born approximation as

$$W_{\mathbf{k}'\mathbf{k}\lambda\lambda} = \frac{2\pi}{\hbar} |\langle \phi_{\mathbf{k}'} | V_{\mathbf{k}'\mathbf{k}} | \phi_{\mathbf{k}} \rangle|^2 \delta(\epsilon_{\mathbf{k},\lambda} - \epsilon_{\mathbf{k}',\lambda'}), \quad (15)$$

where $\phi_{\mathbf{k}}$ and dispersion $\epsilon_{\mathbf{k},\lambda}$ shall be derived from the Hamiltonian of borophene, e.g., Eq. (1).

In order to simplify Eq. (12), a usual route is to approximate the distribution function via an *ansatz* $f = f_0 - e\tau_{\mathbf{k}\lambda} v_{\mathbf{k},\lambda} \mathbf{E} \cdot \frac{\partial f_0}{\partial \epsilon_{\mathbf{k}}}$ with f_0 denotes equilibrium distribution. This allows one to define the relaxation time as

$$\frac{1}{\tau_{\mathbf{k}\lambda}} = \sum_{\mathbf{k}'\lambda'} W_{\mathbf{k}'\mathbf{k}\lambda\lambda} \left(1 - \frac{v_{\mathbf{k}',\lambda'} \tau_{\mathbf{k}'}}{v_{\mathbf{k},\lambda} \tau_{\mathbf{k}}} \right). \quad (16)$$

The wave vectors \mathbf{k} and \mathbf{k}' are two-dimensional wave-vector components, i.e., $\mathbf{k} = k(\cos(\theta), \sin(\theta))$ and $\mathbf{k}' = k'(\cos(\theta'), \sin(\theta'))$. When dealing with an isotropic Fermi surface such as that of graphene, Eq. (16) can be reduced further onto a more simple expression

$$\frac{1}{\tau_{\mathbf{k}\lambda}} = \sum_{\mathbf{k}'\lambda'} W_{\mathbf{k}'\mathbf{k}\lambda\lambda} (1 - \cos(\alpha)), \quad (17)$$

where α is the angle between wave vectors \mathbf{k} and \mathbf{k}' . The relaxation time becomes a function of energy and depends only on the relative angle between momentum wave vector.

For anisotropic Fermi surface, Eq. (17) might still be employed to evaluate the relaxation time and under certain condition should provide a reasonable description of transport as will be further shown below. It will nevertheless yield a less accurate description of scattering events on the Fermi surface. This follows from the observation that the angle between wave vectors \mathbf{k} and \mathbf{k}' as well as their corresponding length changes continuously along nonisotropic Fermi surface. Such variations clearly could not be accommodated by the RTA outlined in Eq. (17). Hence, to get a better estimate of the collision rate between quasiparticles, it is necessary to separate scattering processes on two-dimensional axis by defining relaxation time for x and y direction as τ_x and τ_y , respectively. This is implemented in [33], which also introduced an *ansatz* of distribution function that depends on the electric field and the sum of velocity of Fermi surface from x and y axes. It is shown that upon simplification, one arrives at two set of equations of Fredholm type, which needs to be solved self-consistently.

An alternative route is to define the mean-free path $\Lambda_{\mathbf{k}i}$ for each direction $i = x, y$, which in the RTA amounts to be $\Lambda_{\mathbf{k}i} = v_{\mathbf{k}i} \tau_{\mathbf{k}i}$. The main difference with that discussed in [33] is that we do not need to deal with two variables, i.e., time and velocity but it is sufficient to take care of a single variable $\Lambda_{\mathbf{k}}$, which carries information of collision with accuracies that goes beyond RTA.

Assuming a homogeneous system, we can formulate the Boltzmann's transport in terms of mean-free path. We shall also be assuming that electric field \mathbf{E} sweeps the Fermi surface as $E(\cos(\phi), \sin(\phi))$, whereas the velocity as $v_{\mathbf{k}} = v(\theta)(\cos[\xi(\theta)], \sin[\xi(\theta)])$ for $\xi(\theta)$ being the angle between velocity and unit vector \hat{n} . The latter definition has been made with a consideration that direction of $v(\theta)$ is not necessary the same with that of \mathbf{k} . The Boltzmann's equation can then be simplified by taking an *ansatz*

$$f = f_0 - eE \left(-\frac{\partial f_0}{\partial \epsilon} \right) (\Lambda_x(\theta) \cos(\phi) + \Lambda_y(\theta) \sin(\phi)). \quad (18)$$

Substitution of (18) onto (12) and after using Eq. (14) satisfies two set of equations consisting of

$$\begin{aligned} v(\theta) \cos(\xi[\theta]) &= \tilde{w}(\theta) \Lambda_x(\theta) - \int d\theta' W(\theta, \theta') \Lambda_x(\theta'), \\ v(\theta) \sin(\xi[\theta]) &= \tilde{w}(\theta) \Lambda_y(\theta) - \int d\theta' W(\theta, \theta') \Lambda_y(\theta'), \end{aligned} \quad (19)$$

where short-hand notations $\tilde{w}(\theta) = \int d\theta' W(\theta, \theta')$, and $W(\theta, \theta') = \int dk' k' W_{\mathbf{k}',\mathbf{k}}$ have been used.

It can be deduced from the above equations that a solution of Boltzmann's equation for anisotropic Fermi surface demands for an iterative approaches and its accuracy should be close to an exact solution of Boltzmann's transport equations. Another important feature of the above formulation is that the mean-free path becomes a function of angle and energy, which in contrast to the relaxation time approximation depending only on the energy [see Eq. (17)].

From the knowledge of distribution function or relaxation time, we shall be investigating charge \mathbf{J} and energy \mathbf{Q} current, from which transport coefficients L can be derived. The latter follows from the relation between response and external perturbation as

$$\begin{pmatrix} \mathbf{J} \\ \mathbf{Q} \end{pmatrix} = \begin{pmatrix} L^{aa} & L^{ab} \\ L^{ba} & L^{bb} \end{pmatrix} \begin{pmatrix} \mathbf{E} \\ -\nabla T \end{pmatrix}. \quad (20)$$

In order to express transport coefficients in terms of the mean-free path, we make use again the *ansatz* (18). By fixing the direction of electric field on either $i = x$ or $i = y$ axis, we arrive at the longitudinal coefficients reads

$$\begin{aligned} L_{ii}^{aa} &= e^2 \sum_{\mathbf{k}\lambda} v_{\mathbf{k}\lambda} \Lambda_{\mathbf{k},\lambda i} \cos(\phi - \xi[\theta]) \left(-\frac{\partial f_0}{\partial \epsilon_{\mathbf{k},\lambda}} \right), \\ L_{ii}^{ab} &= e \sum_{\mathbf{k}\lambda} \left(\frac{\epsilon - \mu}{T} \right) v_{\mathbf{k}\lambda} \Lambda_{\mathbf{k},\lambda i} \cos(\phi - \xi[\theta]) \left(-\frac{\partial f_0}{\partial \epsilon_{\mathbf{k},\lambda}} \right), \\ L_{ii}^{bb} &= e \sum_{\mathbf{k}\lambda} \left(\frac{\epsilon - \mu}{T} \right)^2 v_{\mathbf{k}\lambda} \Lambda_{\mathbf{k},\lambda i} \cos(\phi - \xi[\theta]) \left(-\frac{\partial f_0}{\partial \epsilon_{\mathbf{k},\lambda}} \right), \end{aligned} \quad (21)$$

where $v_{\mathbf{k},\lambda}$ being the velocity wave vector and μ denotes the chemical potential. The above equations tell us that a

proper treatment of mean-free path is necessary to accurately derive charge or thermal transport of borophene. In the next section, we shall be discussing the transport coefficients in the presence of short and long-range scatterers and also phonon.

1. Short-range potential

In the absence of substrate, scattering by impurity with short-range potential is expected. The most relevant example in this respect is the fixed defect centers having a potential expressed as a constant $V_{\mathbf{k}\mathbf{k}} = V_0$. Since $V_{\mathbf{k}\mathbf{k}}$ is independent of momenta, the probability amplitude $W_{\mathbf{k}\mathbf{k}}$ does not depend on the angle of wave vectors \mathbf{k} and \mathbf{k}' . This, in turns, simplifies the evaluation of relaxation time in which $1/\tau$ becomes equivalent with a typical expression for isotropic Fermi surface, i.e., only a function of the relative angle between wave vectors, i.e., Eq. (17). This can be directly understood by looking back onto Eq. (16). Setting $W_{\mathbf{k}\mathbf{k}}$ as constant V_0 and using the relation $\theta' \sim \theta + \alpha$, the relaxation time reduces into the form of Eq. (17).

With this caveat in mind, it is thus possible to derive an analytical expression of the longitudinal conductivity by evaluating Eq. (17) together with Eq. (21). Straightforward calculation yields

$$\begin{aligned}\sigma_{xx} &= \frac{e^2}{\hbar} \frac{v_x^3}{v_y V_0^2} s_{0x}, \\ \sigma_{yy} &= \frac{e^2}{\hbar} \frac{v_y^3}{v_x V_0^2} s_{0y},\end{aligned}\quad (22)$$

where $s_{0x} = \frac{\hbar^2 i_{xx}}{2\pi n_{is} a_0}$, $s_{0y} = \frac{\hbar^2 i_{yy}}{2\pi n_{is} a_0}$, with n_{is} being the concentration of impurity of constant potential. We have also defined

$$\begin{aligned}a_0 &= \int d\theta \frac{1 - \cos(\theta)}{\bar{z}^2(\theta)}, \\ i_{xx} &= \int \frac{d\theta}{\bar{z}^2(\theta)} \frac{\cos^2(\theta)}{I_0^2(\theta)}, \\ i_{yy} &= \int \frac{d\theta}{\bar{z}^2(\theta)} \left[\frac{\sin(\theta)}{I_0(\theta)} + \frac{v_F v_t}{v_y^2} \right]^2.\end{aligned}\quad (23)$$

where $\bar{z}(\theta)$ and $I_0(\theta)$ are defined in Eq. (7) and Eq. (8), respectively. It is clear that conductivity of borophene with short-range impurity is independent of momentum or energy, meaning that it remains unaffected by variation of charge doping. A rather similar result has also been shown for graphene as outlined in [34]. We note that the absence of doping dependence in the above expression stems from the deficiency of Boltzmann transport, which only includes Born-type correction. An improvement is usually achieved by going beyond Boltzmann analysis, e.g., via perturbation expansion of higher order. The hallmark of the above expression is the discrepancy of conductivity along the x and the y axes, which is evident through a dependence of conductivity on the velocities v_x and v_y . As we shall further observe in the following sections, such behavior persists in the presence of long-range impurity with and without electron-phonon coupling.

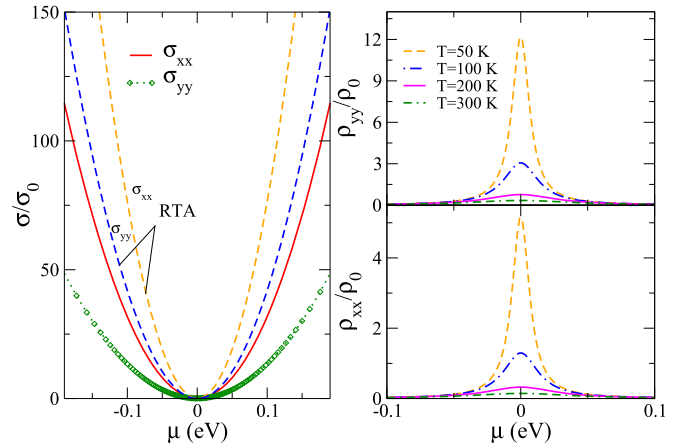


FIG. 2. (Left panel) Longitudinal conductivity σ_{xx} and σ_{yy} of borophene in unit of $\sigma_0 = e^2/h$ at $T = 50$ K. Dashed lines correspond to the results derived via relaxation time approximation (RTA) for both x and y directions. (Right panels) Variation of resistivity ρ in unit of $\rho_0 = 1/\sigma_0$ along the y (top panel) and x direction (bottom panel).

2. Long-range potential

When defect centers consist of an internal structure such as an ionized point impurity with charge Ze , the potential of isolated scatterers is of Coulomb type $V(r) = \frac{Ze^2}{4\pi\epsilon_r\epsilon_0 r}$, with Z being the valence number, ϵ_r denotes the average dielectric constant and $\epsilon_0 = 8.85 \times 10^{-12}$ C/Vm being the vacuum permittivity. The bare potential $V(r)$ spans over a large distance r , starting from the locus of each point charge impurity. This behavior, however, does not generally hold for semimetallic system such as borophene since the excess potential is usually screened by conduction electrons. In the event that a large number of carrier and impurity are weakly coupled, it is sufficient to consider a screening effect within the Thomas-Fermi approximation, which constitutes of improving the bare potential through a factor of $e^{-\delta r}$ with $1/\delta$ being the screening radius. By incorporating screening effect, Fourier transformation of the potential $V(r)$ yields

$$V(\mathbf{k}, \mathbf{k}') = \frac{Ze^2}{4\bar{\epsilon}_r} \frac{1}{|\mathbf{k} - \mathbf{k}'| + \delta_{\mathbf{q}}}, \quad (24)$$

where $\bar{\epsilon}_r = \epsilon_r\epsilon_0$ and $\delta_{\mathbf{q}} = e^2 D(\epsilon)/\bar{\epsilon}_r$ being the Thomas-Fermi screening vector. Electronic and thermal transport with long-range Coulomb impurity can now be investigated by combining Eq. (24) together with Eq. (19).

Below, unless otherwise stated, we shall be describing our results at a constant impurity density $n_i = 5 \times 10^{12}/\text{m}^2$. We use $Z = 1$ and $\epsilon_r \sim 1$, which describes impurity on the suspended borophene. This in contrast with that in [32], in which ϵ_r is set at around 2.5 by assuming SiO_2 as a substrate. In the present paper, we shall be including correction to ϵ_r when discussing transport in the presence of polar substrate.

Let us begin our discussion by looking at the conductivity as a function of doping, which is plotted in Fig. 2. As is readily seen, the conductivity on both axes grows quadratically together with chemical potential, which implies for an enhancement of conductivity when sample consists of a large

number of carriers. Along with this, the conductivity of the x direction is almost two-times larger in magnitude than that in the y direction, which is particularly true for $|\mu| > 0.1$ eV.

The origin of such behavior could be made clear by evaluating the conductivity in the relaxation time approximation, which allows for analytical derivation of scattering lifetime. Carrying out integrals on Eq. (17), we get $\frac{1}{\tau_{\mathbf{k}}} = \frac{V_0^2 \pi z_0}{\hbar^2 v_F k}$, which is equivalent for both x and y axes. Using this in Eq. (21) and setting $\Lambda_{\mathbf{k}} = \bar{v}_{\mathbf{k}} \tau_{\mathbf{k}}$ together with $\cos(\phi - \xi[\theta]) = 1$ yields conductivity near zero temperature as

$$\begin{aligned}\sigma_{xx} &= \frac{e^2}{\hbar} \frac{\mathcal{S}_{0x}}{V_0^2} \mu^2, \\ \sigma_{yy} &= \frac{e^2}{\hbar} \frac{\mathcal{S}_{0y}}{V_0^2} \mu^2,\end{aligned}\quad (25)$$

where $V_0 = \frac{\sqrt{n_i} Z e^2}{4\pi \epsilon_r}$, with n_i denotes charge density of impurities and dimensionless parameters: $z_0 = \int d\theta \frac{1}{z(\theta)}$,

$$\begin{aligned}\mathcal{S}_{0x} &= \frac{v_x^2}{v_y^2} \frac{I_{xx}}{z_0}, \\ \mathcal{S}_{0y} &= \frac{v_y^2}{v_x^2} \frac{I_{yy}}{z_0}, \\ I_{xx} &= \int \frac{d\theta}{z^3(\theta)} \frac{\cos^2(\theta)}{I_0^2(\theta)}, \\ I_{yy} &= \int \frac{d\theta}{z^3(\theta)} \left[\frac{\sin(\theta)}{I_0(\theta)} + \frac{v_F v_t}{v_y^2} \right]^2.\end{aligned}\quad (26)$$

The above equations tell us that in the RTA the quadratic dependence of conductivity on doping arises from the energy-dependent lifetime. The anisotropy of conductivity on the other hand is not affected by scattering lifetime, by recalling that we have employed the same expression on both axes, but through nonuniform Fermi velocities v_x and v_y as prefactors of I_{xx} and I_{yy} variables. By using this observation, one could further deduce that the conductivity remains anisotropic even in the absence of the tilted velocity. Our calculation also suggested that in the absence of the latter the conductivity tends to be smaller than that with finite tilted velocity.

In contrast to the RTA, the anisotropy and quadratic power law of conductivity in the perspective of the self-consistent Boltzmann calculation arises directly from the mean-free path Λ_{xx} and Λ_{yy} . This is clear since they record simultaneously variations on both angle and energy during self consistency iteration.

The anisotropy of conductivity, interestingly, carries on when the number of charged impurity doping approaches carrier number, which is usually taken as a low-doping regime. This can be shown from Eq. (25) in which the conductivity at $n \sim n_i$ could be rewritten as

$$\begin{aligned}\sigma_{xx} &= \frac{4e^2}{h} \frac{\mathcal{S}_{0x}}{D_0}, \\ \sigma_{yy} &= \frac{4e^2}{h} \frac{\mathcal{S}_{0y}}{D_0}.\end{aligned}\quad (27)$$

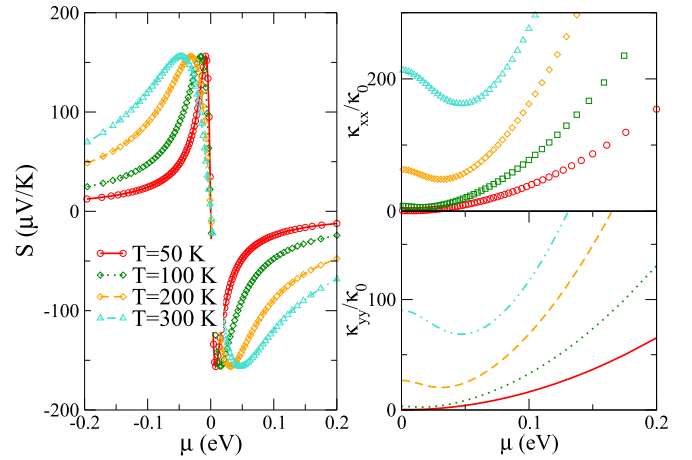


FIG. 3. Left panel shows thermopower of borophene for x and y axes whereas right panels consist of thermal conductivity for x (upper panel) and y (lower panel), in unit of $\kappa_0 = k_B eV/h$.

The discrepancy of conductivity around zero doping estimated above via relaxation time approximation is indeed supported by the solution of self-consistent Boltzmann's equation. To see this aspect more clearly we show in the right panels of Fig. 2 the calculated resistivity for temperature range 50–300 K. At the charge neutrality point the resistivity appears to be nonuniform on both axes and this is independent of temperature. In addition, we also observe that resistivity, similar to that is seen in conductivity, along the y axis (upper-right panel) is larger almost two times in magnitude than that of x axis (lower-right panel). It is important to note, however, that Eqs. (27) might overestimate the conductivity near zero doping, which could be understood since RTA only accounts for energy dependence.

When temperature gradient is generated on the sample, we can measure a thermopower, i.e., Seebeck coefficient, which arises due to an internal electric field built up by the spatial variation of charge. Thermopower derived via self-consistent equations is plotted in the left panel of Fig. 3, which holds for $T = 50$ K up to 300 K. It changes according to $-\frac{1}{\mu}$, reaches a maxima near $\mu \rightarrow 0$, and then gradually decreases when chemical potential gets larger. The former suggests that at smaller doping large thermopower arises due to ease formation of charge imbalance while the latter describes the opposite case. Negative thermopower corresponds to hole carriers moving in the opposite direction of heat flow whereas positive thermopower describes electron moving along heat energy.

The asymmetry of the Seebeck's coefficient with respect to chemical potential follows the standard Mott's formula, which connects the conductivity and thermopower as

$$S_{ii} = -\frac{\pi^2 k_B^2 T}{3e} \frac{\partial}{\partial \mu} \ln \sigma_{ii}(\mu), \quad (28)$$

where i denotes x and y axes. While the above formula correctly predicts linear T , it, however, fails to describe the absence of anisotropy in the thermopower, which should be easily realized since S depends only on the derivative of σ . As is readily seen, the thermopower on the x and y axes in Fig. 3

are, hardly distinguishable and this holds for different carrier density and various temperature range.

In order to understand the behavior of thermopower derived from self-consistent equations, we could again implement the RTA to derive the off-diagonal coefficients. By following the same step as outlined above for the conductivity, one readily derives

$$\begin{aligned} L_{xx}^{12} &= -\frac{e k_B^2 T}{\hbar V_0^2} \mu \mathcal{S}_{0x}, \\ L_{yy}^{12} &= -\frac{e k_B^2 T}{\hbar V_0^2} \mu \mathcal{S}_{0y}. \end{aligned} \quad (29)$$

They depend on the orientation similar to that of conductivity. To obtain the thermopower, we can combine the above equations with those in Eqs. (25) via $S = \frac{L^{ab}}{L^{aa}}$. They yield $\sim -\frac{1}{\mu}$ dependence, which is uniform for both directions. Thus, albeit L^{aa} and L^{ab} depends on x and y axes through velocities and angle integral, these anisotropic parameters are canceled out and do not affect thermopower. In addition to this, the linear temperature dependence explains the shift of S along with temperature.

In order to complement the above discussion, let us examine the thermal conductivity, which is shown in the right panels of Fig. 3 for various temperature. While thermopower is independent of orientation, the thermal conductivity $\kappa = L^{bb} - (L^{ab})^2/L^{aa}$ shows a rather different behavior namely that κ in the x direction is generally larger than that in the y direction, which is similar to that of conductivity. The similarity between κ and σ as doping varies apparently follows from

$$\kappa = \frac{1}{2} c_e v \Lambda, \quad (30)$$

which also depends on the mean-free path Λ . On top of this, we also observe that thermal conductivity initially decreases at low doping but subsequently increases along with carrier density. Nonmonotonous dependence of thermal conductivity near zero doping, which, as further discussed below, implies for unusual characteristic of transport.

In order to establish a solid ground for the latter argument, we complement the above results with the Lorenz ratio $L = \frac{\kappa}{T\sigma}$ as displayed in the left panel of Fig. 4. To understand the plots, we first recall that for metallic gas, the ratio between thermal and charge conductivity obeys the law of Wiedemann-Franz in which L is proportional to a constant number namely $L_0 = \frac{\pi^2}{3} \left(\frac{k_B}{e}\right)^2 = 2.44 \times 10^{-8} \text{ V}^2/\text{K}^2$. At large carrier density, it is noticeable that the Wiedemann-Franz's law is respected by the self-consistent calculation suggesting that carrier behaves like those in an ideal metallic gas. At smaller doping $|\mu| < 0.1 \text{ eV}$ on the other hand, the Lorenz ratio increases beyond L_0 and this appears at low up to high temperature.

To fully understand the Lorenz ratio, particularly at the charge neutrality point, it is instructive to derive L/L_0 from the perspective of the RTA, which also allows for analytical derivation. This can be achieved by using Eq. (30) together with the specific heat derived in Eq. (10). Let us rewrite Eq. (30) as $\kappa = \frac{1}{2} c_e \bar{v}_i \Lambda_{ii}$, with \bar{v} denotes the root-mean-square velocity for each i axis. Using this formula together with Eq. (10), one readily writes the direction-dependent

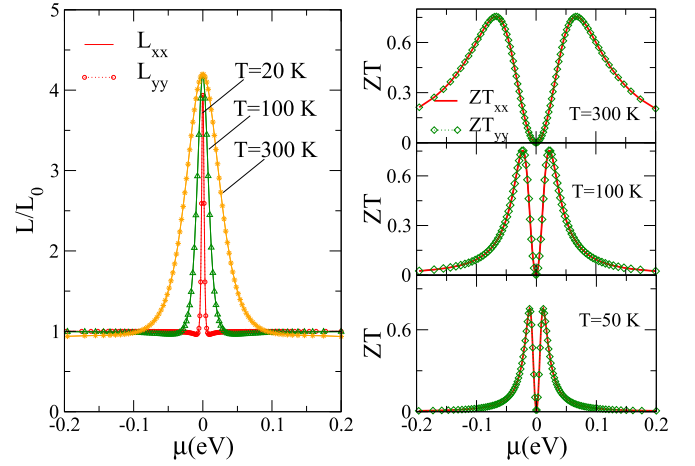


FIG. 4. Left panel consists of the Lorenz ratio for both x and y directions in unit of $L_0 = 2.44 \times 10^{-8} \text{ V}^2/\text{K}^2$ and for various temperature. In the right panel, figure of merit ZT for x and y axes are calculated from $T = 50 \text{ K}$ (bottom panel) up to $T = 300 \text{ K}$ (top panel).

thermal conductivity as

$$\begin{aligned} \kappa_{xx} &= \frac{108 \zeta(3) \ln(2) k_B^2 T}{\pi \hbar} \frac{\sqrt{v_x} \mathcal{S}_{0x} \bar{V}_{0x} \mathcal{M}_0}{\sqrt{v_y} D_0}, \\ \kappa_{yy} &= \frac{108 \zeta(3) \ln(2) k_B^2 T}{\pi \hbar} \frac{\sqrt{v_y} \mathcal{S}_{0y} \bar{V}_{0y} \mathcal{M}_0}{\sqrt{v_x} D_0}, \end{aligned} \quad (31)$$

where $\mathcal{M}_0 = \frac{I_0(\theta)}{\bar{z}(\theta)}$, $\bar{V}_{0x} = \sqrt{V_{0x}}$, $\bar{V}_{0y} = \sqrt{V_{0y}}$, and

$$\begin{aligned} V_{0x} &= \frac{1}{2\pi} \int d\theta \frac{\cos^2(\theta)}{I_0^2(\theta)}, \\ V_{0y} &= \frac{1}{2\pi} \int d\theta \left[\frac{\sin(\theta)}{I_0(\theta)} + \frac{v_t v_F}{v_y^2} \right]^2, \end{aligned} \quad (32)$$

In deriving the above equations, we have made use of the mean-free path in the form of

$$\begin{aligned} \Lambda_{xx} &= 24 \ln(2) \frac{\hbar v_F}{k_B T} \frac{\mathcal{S}_{0x} I_0(\theta)}{D_0} \sqrt{\frac{v_y}{v_x}}, \\ \Lambda_{yy} &= 24 \ln(2) \frac{\hbar v_F}{k_B T} \frac{\mathcal{S}_{0y} I_0(\theta)}{D_0} \sqrt{\frac{v_x}{v_y}}, \end{aligned} \quad (33)$$

for x and y axis, respectively. These expressions have been derived by comparing the conductivity near zero doping, i.e., Eq. (27) with the standard expression of conductivity for electronic gas, i.e., $\sigma_{ii} = \frac{ne^2 \Lambda_{ii}}{mv}$ [35]. This approach, albeit an approximation, enable us to derive an axis-dependent mean-free path, which is necessary to detect the influence of the anisotropy of Λ on the Lorenz ratio. Evaluation of $L_{ii} = \frac{\kappa_{ii}}{T\sigma_{ii}}$ could then be carried out straightforwardly giving

$$\begin{aligned} L_{xx} &= \frac{108 \ln(2) \zeta(3)}{\pi} \left(\frac{k_B}{e}\right)^2 \sqrt{\frac{v_x}{v_y}} \frac{\bar{V}_{0x} \bar{\mathcal{M}}_0}{D_0} = 4.34 L_0, \\ L_{yy} &= \frac{108 \ln(2) \zeta(3)}{\pi} \left(\frac{k_B}{e}\right)^2 \sqrt{\frac{v_y}{v_x}} \frac{\bar{V}_{0y} \bar{\mathcal{M}}_0}{D_0} = 5.83 L_0, \end{aligned} \quad (34)$$

where $\bar{\mathcal{M}}_0 = \int d\theta \mathcal{M}_0$.

Let us collect our results outlined above. Eq. (31) demonstrates that the thermal conductivity of dirty borophene in the perspective of the RTA is indeed anisotropic and results from the disparity of mean-free path and Fermi velocities. This is in a good agreement with that plotted in Fig. 3 derived via self-consistent calculation. From Eq. (34), we learn further that at the charge neutrality point, the Lorenz ratio becomes several times larger than L_0 and independent of temperature, which certainly corroborates with that shown in Fig. 4. The above analytical results, however, slightly overestimates the numerical value of L/L_0 due to an approximation in the derivation of the mean-free path, which leads to a small discrepancy between that of x and y axes. Although RTA correctly predicts the notion that L_{xx}/L_0 and L_{yy}/L_0 at charge neutrality point should be close numerically, they remains contradicts with that obtained via self-consistent calculation, which yields the same value of L/L_0 on both axes.

Going back to L/L_0 plotted in the left panel Fig. 4, we find that a complete violation Wiedemann-Franz's appears when borophene is slightly doped, i.e., at the vicinity of charge neutrality point in which the Lorenz number changes along with doping and depends on temperature. In addition, we find that at room temperature 300 K, the amount of charge dopants required to induce metallic state is larger than that at lower temperature $T < 100$ K. This might arise from a parabolic dependence of thermal conductivity around $\mu = 0.1$, which does not appear below $T = 300$ K.

In view of the above results, we recall that violation of Wiedemann-Franz's law is usually expected whenever phonon scattering or electron interaction is taken into account. Since they are absent in the present calculation, anomaly at low density hints at a transport mechanism that differs from a typical metallic gas and its origin should only involve electrons. Variation of Lorenz ratio $\frac{L}{L_0}$ from 1 to 4 could therefore be translated as a crossover from metallic gas to an interacting like electron gas. This interpretation corroborates with the behavior of resistivity discussed previously, which is pronounced at low doping but subsequently decay at larger carrier density. There are two possible scenarios that could be used to explain a deviation from metallic gas at low doping and to pinpoint the origin of anomaly in both κ and L . The most simple scenarios is impurity induced scattering, which might be understood directly by looking at the RTA expressed in Eq. (27). It states that a small conductivity is true when σ linearly depends on n and inversely proportional to n_i . This implies that at low n , carrier is effectively scattered by impurity, subsequently reduces probability of charge transport, leading to an increase of resistivity.

Another possible scenario is, perhaps, a Dirac fluid in which an ensemble of electron resembles viscous liquid and might exhibit various phenomena known in the classical hydrodynamics. This has been proposed in the context of graphene to explain the violation of Wiedemann-Franz's law and also the cusp in the thermal conductivity, which do not fully explicable with the above simple picture. Recent experiments along this line have been discussed in [36,37]. Due to the similarity of low energy between graphene and borophene, one might expect that characteristic of electron of borophene at low doping may resemble a Dirac fluid. However, this

is currently an open question and a quantitative comparison among possible scenarios is necessary to get the most suitable picture.

Equipped with the knowledge of transport, we can go further to assess the performance of monolayer borophene as a thermoelectric device. A standard approach to do this is to measure the figure of merit (FOM) as $ZT = \alpha^2 \sigma / \kappa$, which quantifies the competition between electrical and thermal conductivity. In the right panels of Fig. 4, we plot the figure of merit (FOM), which is calculated from 50 K up to 300 K. As can readily be seen, the FOM consists of zero at $\mu = 0$, increases up to a maximum value of ≈ 0.8 but subsequently decreases when doping gets larger. A zero ZT at $\mu = 0$ emerges from the suppression of conductivity whereas maxima and rapid decay at high doping follows from that of thermopower and rapid increase of thermal conductivity along with chemical potential. By increasing temperature, we find a broadening of ZT , which reflects that conversion efficiency of doped borophene at $T = 300$ K should be better than that at 50 K. We can thus deduce that dirty borophene consists of long-range scatterer has a promising potential for thermoelectric component by considering that it has a value of ZT close to the order of $\rightarrow 1$, which prevails up to a room temperature. This resembles a typical efficiency of a well-known thermoelectric material widely used today. It is important to note, however, that experimental realization of this finding seems to be difficult. At high temperature another aspect need to be considered is the influence of phonon, which might arise intrinsically or via a coupling with an atom of a substrate.

IV. TRANSPORT WITH INELASTIC SCATTERING

In order to elaborate the foregoing analysis, we move on to discuss the role of inelastic process, which is essential for a realistic description of electronic properties of supported borophene. It is generally expected that transport in the low-dimensional system is affected by not only impurities but also vibration modes that is coupled with electron. The most relevant contribution comes from the in-plane longitudinal acoustic or optical branch, which correspond to a small displacement of atoms of borophene that is coupled with atoms of substrate.

From first-principle calculation, we learn that scattering by the in-plane longitudinal acoustic remains important even at low temperature. This is attested by the acoustic phonon energy that spans from ground state up to 41 meV [11]. Optical phonon on the other hand lies above at higher energy, approximately up to 165 meV, suggesting that its contribution is minimal and could be neglected when one is interested in transport at low up to room temperature. Another possible contribution arises from the remote phonon scattering, which corresponds to the optical phonon branch of high dielectric substrate. Its influence is expected to be non-negligible even at room temperature and has been considered as an important factor that inhibits charge mobility.

In the standard Boltzmann's formalism, interaction between electron and phonon enters via collision rate. It now constitutes of contributions from point impurities and

electron-phonon interaction, which can be summed linearly as

$$\left. \frac{\partial f_{\mathbf{k},\lambda}}{\partial t} \right|_{c,i-ph} = \left. \frac{\partial f_{\mathbf{k},\lambda}}{\partial t} \right|_{\text{imp}} + \sum_i \left. \frac{\partial f_{\mathbf{k},\lambda}}{\partial t} \right|_{i,e-ph}. \quad (35)$$

where i denotes acoustic or polar optical contribution. The impurity related collision can be evaluated via Eq. (14) whereas electron-phonon interaction requires Eq. (13). The latter contains the transition probability $W_{\mathbf{k}\mathbf{k}'}$, connecting wave vectors \mathbf{k} and \mathbf{k}' reads

$$W_{\mathbf{k}\lambda\mathbf{k}'\lambda'} = \frac{2\pi}{\hbar} M_{\mathbf{k}\mathbf{k}'} [n_{\mathbf{q}} \delta(\epsilon_{\mathbf{k},\lambda} - \epsilon_{\mathbf{k}',\lambda'} - \epsilon_{\mathbf{q}}) + (n_{\mathbf{q}} + 1) \delta(\epsilon_{\mathbf{k},\lambda} - \epsilon_{\mathbf{k}',\lambda'} + \epsilon_{\mathbf{q}})], \quad (36)$$

with matrix elements $M_{\mathbf{k}\mathbf{k}'}(\mathbf{q}) = |\langle \phi_{\mathbf{k}'} | H_{e-ph,\mathbf{k}'\mathbf{k}} | \phi_{\mathbf{k}} \rangle|^2 \delta_{\mathbf{k}',\mathbf{k}+\mathbf{q}}$ for H_{e-ph} being the Hamiltonian of electron-phonon interaction. The wave vectors \mathbf{k} and \mathbf{k}' obeys the conservation of momentum within the reciprocal lattice, i.e., $\mathbf{k}' = \mathbf{k} + \mathbf{q}$ with \mathbf{q} being the wave vector of two-dimensional phonon. The phonon dispersion energy is defined as $\epsilon_{\mathbf{q}}$ whereas $n_{\mathbf{q}}$ being the phonon distribution function. In the above notation, $n_{\mathbf{q}}$ represents phonon absorption and $n_{\mathbf{q}} + 1$ describes emission. We have also assumed that lattice vibration induces only a weak perturbation on electrons.

Implementation of self-consistent solution of Boltzmann's equations in the presence of inelastic scattering is more involved and time consuming, particularly for deriving T dependence observable. In order to deploy Eq. (19), we need first to simplify the collision term. Starting with Eq. (13), we may reduce the expression onto a manageable form by neglecting Pauli term yielding

$$\left. \frac{\partial f_{\mathbf{k},\lambda}}{\partial t} \right|_c = \sum_{\mathbf{k}'\lambda'} [W_{\mathbf{k}'\lambda'\mathbf{k}\lambda} f_{\mathbf{k}',\lambda'} - W_{\mathbf{k}\lambda\mathbf{k}'\lambda'} f_{\mathbf{k},\lambda}]. \quad (37)$$

When the effect of electron-phonon scattering does not results in a large deflection of wave vector so much that $\mathbf{k} \sim \mathbf{k}'$, is still satisfied, the above expression might be further reduced onto the form Eq. (14). This greatly simplifies Boltzmann's transport equation Eq. (12) such that one may derive equations for the mean-free path in the form of Eq. (19), with $\tilde{w}(\theta)$ now takes account of the electron-phonon matrix, i.e., Eq. (36).

Having simplified the Boltzmann's equation, it is necessary to mention two possible ways to evaluate the effective mean-free path, which records scattering off impurity and lattice vibration, that will be used to evaluate transport coefficients. The first is to solve Eq. (19) for each process and then proceed to derive the effective mean-free path via inverse summation of each contribution as $\Lambda^{-1} = \sum_i \Lambda_i^{-1}$, where i denotes contribution of impurity and phonon. Alternatively we might derive the mean-free path directly by incorporating all contributions in the form of Eq. (35). In this way we shall be arriving at the same expression equivalent to that Eq. (19), with $\tilde{w}(\theta)$ contains both impurity and electron-phonon contribution. Our calculation shows that both approaches yield qualitatively the same results although slightly differ quantitatively. In the present paper, we shall be applying the first approach to derive the effective mean-free path in the presence of impurity, acoustic and polar optical phonon.

A. Acoustic phonon

Let us now examine the interaction between electron and acoustic phonon mode whose impact is expected to hold even at low temperature. At long-wavelength limit, the in-plane coupling between electron and acoustic phonon H_{e-ac} might be determined via deformation potential approximation. A small displacement of ion amounts to inducing a potential in the form of $\Delta V = \nabla \mathbf{u}$ where $\mathbf{u} = \sqrt{\frac{\hbar}{2\rho_B A \omega_{\mathbf{q}}}} \hat{\mathbf{e}}_{\mathbf{q}} (a_{\mathbf{q}} + a_{-\mathbf{q}}^\dagger)$ being the displacement vector and $a(a^\dagger)$ being annihilation (creation) operators of phonon. ρ_B denotes the density of monolayer borophene, A is the area of the sample and $\omega_{\mathbf{q}} = v_s \mathbf{q}$ being the long-wavelength dispersion of acoustic phonon with v_s denotes the velocity of sound. The interaction between electron and lattice vibration mode in the form of $H = D_A \Delta V$ takes an explicit expression as

$$H_{e-ac} = D_A \sqrt{\frac{\hbar}{2\rho_B A \omega_{\mathbf{q}}}} \hat{\mathbf{e}}_{\mathbf{q}} \cdot \mathbf{q} (a_{\mathbf{q}} + a_{-\mathbf{q}}^\dagger), \quad (38)$$

where D_A is the deformation-potential coupling.

Before discussing the results of the self-consistent relation, it is instructive to simplify the Boltzmann's equation onto a more manageable form, which shall give us a better insight on the structure of the equation. By recalling the relaxation time approximation, we shall be using the *ansatz* in the form of $f = f_0 - e\tau_{\mathbf{k}\lambda} v_{\mathbf{k},\lambda} \mathbf{E} \cdot \frac{\partial f_0}{\partial \mathbf{k}}$. The relaxation time $\tau_{\mathbf{k}}$ might then be derived by way of Eqs. (16) and (36) together with Eq. (38) giving

$$\frac{1}{\tau_{\mathbf{k}\lambda}} = \frac{2\pi}{\hbar} \sum_{\mathbf{q}\mathbf{k}'\lambda'} M_{\mathbf{k}\mathbf{k}'} \left[1 - \frac{v_{\mathbf{k}',\lambda'} \tau_{\mathbf{k}'\lambda'}}{v_{\mathbf{k},\lambda} \tau_{\mathbf{k}\lambda}} \right] (n_{\mathbf{q}}^0 \delta(\epsilon_{\mathbf{k},\lambda} - \epsilon_{\mathbf{k}',\lambda'} - \epsilon_{\mathbf{q}}) + (n_{\mathbf{q}}^0 + 1) \delta(\epsilon_{\mathbf{k},\lambda} - \epsilon_{\mathbf{k}',\lambda'} + \epsilon_{\mathbf{q}})), \quad (39)$$

where $n_{\mathbf{q}}^0 = (\exp(\hbar\omega_{\mathbf{q}}/(k_B T)) - 1)^{-1}$ being the phonon occupation number in the equilibrium whereas electron-phonon matrix takes the form of

$$M_{\mathbf{k}\mathbf{k}'} = \frac{D_A^2}{4\rho_B A} \frac{\hbar \mathbf{q}^2}{\omega_{\mathbf{q}}} (1 + \cos(\theta_{\mathbf{k}} - \theta_{\mathbf{k}'})). \quad (40)$$

Equation (39) could be further simplified by assuming only the quasi-elastic collision whose analytical solution can be derived at two different limits, viz., high- and low-temperature regime, which we shall be looking in more detail below.

From the theory of solids, it is well known that for a system with electron phonon-coupling, the high- and low-temperature regimes might be separated by a scale such as Debye T_D or Grüneisen T_{BG} temperature, whichever that is lowest. Currently, it is not, however, possible to supply an accurate value of T_D due to the absence of experiment on 8-*Pmmn* borophene. The Bloch-Grüneisen temperature on the other hand, can be estimated from the relation $T_{BG} \sim 2\hbar v_s k_F / k_B$ where k_F being a wave vector expressed in Eq. (9). Since k_F of borophene depends on the angle θ we shall be estimating T_{BG} in our discussion below by using the lowest to highest possible values. We note in passing that while the T_{BG} may not be an exact boundary between high- or low-temperature regime, in which electron-phonon coupling could behave differently, it nevertheless provides useful estimate of

the dependence of transport coefficient on temperature and could be compared with that via self-consistent calculation.

At high temperature, $T \gg T_{BG}$, Eq. (39) can be reduced by noting that bosonic occupation number can be written as $n_{\mathbf{q}}^0 \approx k_B T / \hbar \omega_{\mathbf{q}}$. This, together with the elastic approximation $\epsilon'_{\mathbf{k}} - \epsilon_{\mathbf{k}} \pm \epsilon_{\mathbf{q}} \approx \epsilon'_{\mathbf{k}} - \epsilon_{\mathbf{k}}$, gives

$$\frac{1}{\tau_{\mathbf{k}\lambda}} = \frac{\pi D_A^2 k_B T}{\rho_B \hbar^2 v_s^2 v_F} \sum_{\mathbf{k}'\lambda'} \left[1 - \frac{v_{\mathbf{k}'\lambda'} \tau_{\mathbf{k}'\lambda'}}{v_{\mathbf{k},\lambda} \tau_{\mathbf{k}\lambda}} \right]. \quad (41)$$

When the anisotropy of the Fermi surface is neglected, we can evaluate the above integral by taking account only the angle between wave vectors. The conductivity can then be derived by using the above integral together with Eq. (21) giving

$$\begin{aligned} \sigma_{xx} &= \frac{e^2 v_x^3}{\hbar v_y} \frac{\rho_B \hbar^2 v_s^2}{\pi D_A^2 k_B T c_0} i_{xx}, \\ \sigma_{yy} &= \frac{e^2 v_y^3}{\hbar v_x} \frac{\rho_B \hbar^2 v_s^2}{\pi D_A^2 k_B T c_0} i_{yy}, \end{aligned} \quad (42)$$

with $c_0 = \int d\theta \frac{\sin^2(\theta)}{\bar{z}(\theta)^2}$, resembling that obtained with constant potential with an exception that the above expressions depend on the electron-phonon coupling and inversely proportional to temperature. Note that a rather similar linear dependence at high temperature is also obtained for graphene [34].

When measurement of transport is performed at the Bloch-Grüneisen regime, i.e., $\hbar \omega_{\mathbf{q}} \sim k_B T$, we shall be dealing with the possibility of degeneracy, which means that phonon distribution function should be kept intact so as to preserve the character of bosonic distribution. By introducing a dimensionless variable $x = \hbar \omega_{\mathbf{q}} / k_B T$, Eq. (39) can be casted onto

$$\frac{1}{\tau_{\mathbf{k}\lambda}} = \tilde{D}_A \sum_{\lambda'} \int dx \frac{x^4}{2k^2} \left[1 - \frac{v_{\mathbf{k}'\lambda'} \tau_{\mathbf{k}'\lambda'}}{v_{\mathbf{k},\lambda} \tau_{\mathbf{k}\lambda}} \right] n_x^0 (n_x^0 + 1), \quad (43)$$

where $\tilde{D}_A = \frac{D_A^2 \pi}{\rho_B v_s} \left(\frac{k_B T}{\hbar v_s} \right)^4$. As previously shown, under a condition of circular Fermi surface, i.e., neglecting the anisotropy of Fermi wave vectors, we can simplify the terms under the bracket with a summation over an angle between wave vectors. Direct evaluation yields $1/\tau = \tilde{D}_A \frac{\hbar v_F^4 \zeta(4)}{E_F^2}$, which takes a similar form with that obtained for graphene [38]. The important caveat of τ is the nonlinear temperature dependence, which also implies that the resistivity due to acoustic phonon should change according to T^4 at low temperature. Further comment on this aspect will be outlined below when discussing the result derived via self-consistent calculation.

In what follows, we shall be discussing the results of transport in the presence of long-range charge impurities together with the acoustic phonon. In the numerical implementation, we have made use a number of parameters as follows: the density of borophene is set constant at the order $\rho_B = 10^{-8} \text{ g/cm}^2$, whereas the longitudinal acoustic velocity is $v_s = 10^6 \text{ cm/s}$. The deformation potential D_A on the other hand has been estimated by following the deformation potential theory outlined in [31], which derives $D_A = S_1 + v_t / v_y E_\beta \sin(\theta_m)$ for S_1 being a multiplicative factor of strain ϵ_{strain} , E_β denotes deformation hopping constant and θ_m is direction of Dirac point upon shifted by strain. All these parameters could be derived from first-principles calculations and yields D_A within the range

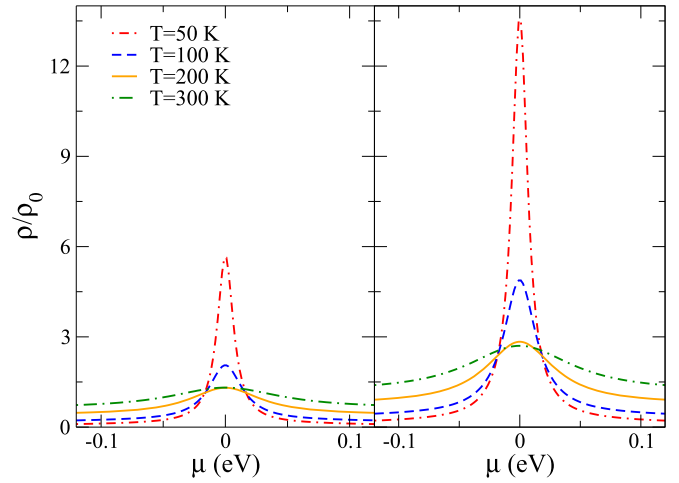


FIG. 5. Variation of resistivity in unit $\rho_0 = 1/\sigma_0$ for x (left panel) and y (right panel) direction calculated at $D_A = 2 \text{ eV}$ and various temperature.

of 0.18–2.16 eV. Since this value should be compared with experimental data, which are currently lacking, we shall be varying D_A from 2 eV up to 16 eV. This choice has been made to give a clear description of signature of electron-phonon interaction at various strength of coupling and to accommodate possible discrepancy between theoretical estimate and experimental observation.

Let us examine the result of resistivity as a function of doping, which is depicted in Fig. 5. At small doping, the resistivity becomes slightly larger than that is seen in Fig. 2 and it decreases when temperature increases. At larger doping, on the other hand, the resistivity shifts toward larger values together with temperature. This is in contrast to that in Fig. 2, which does not depend on temperature at higher doping. A shift of both ρ_{xx} and ρ_{yy} toward larger values as temperature increases seems to corroborate with the formula derived within RTA in Eq. (42). The inclusion of lattice vibration amounts to reducing the mean-free path traveled by carriers, which results in the increase of resistivity at low to high doping concentration. That this behavior is enhanced at low temperature indeed demonstrates the non-negligible impact of acoustic phonon and should be incorporated in the realistic description of charge transport of borophene. It is interesting to mention that the dependence of resistivity on temperature at high doping resembles that is observed experimentally on two-dimensional system, such as graphene [39].

The signature of electron-phonon coupling could be further realized from the temperature-dependent resistivity at a constant number of carrier. This is depicted in Fig. 6. As expected, the resistivity increases along with temperature and the discrepancy between x and y direction persists for all n and T . At low temperature, we observe a quartic power law, which goes along with RTA formulation outlined Eq. (43). At a carrier density $n = 2 \times 10^{12} / \text{cm}^2$ the T^4 dependence goes up to $T = 40 \text{ K}$, which seems to be in accord with the Grüneisen temperature in the range of $40 < T_{BG} < 54 \text{ K}$. A good agreement is also shown when charge carrier is set at $n = 3 \times 10^{12} / \text{cm}^2$ in which the quartic dependence falls within the Grüneisen temperature $60 < T_{BG} < 81 \text{ K}$. From the perspective of the

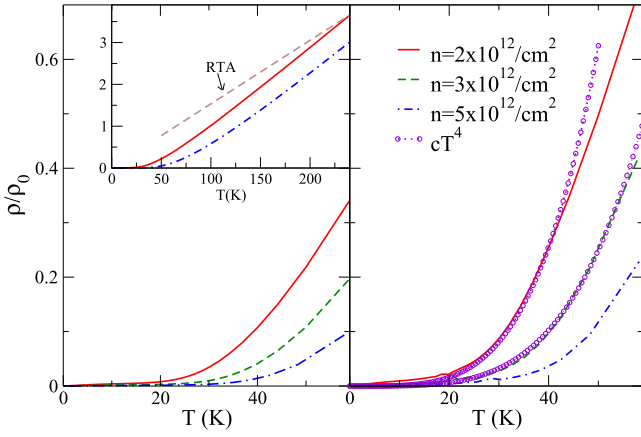


FIG. 6. Temperature-dependent resistivity calculated at $D_A = 8$ eV for different number of charge carrier n . Left and right panels describe resistivity along the x and y direction, respectively. The inset in the left panel displays the same lines plotted in the main panel but with a larger scale of temperature. Dashed line shows the estimate of resistivity at high temperature via relaxation time approximation. In the right panel, dashed-circled lines correspond to cT^4 with c being constant, which is derived from the T_{BG} estimate.

well-known relation $\rho(T) = \rho_{\text{imp}} + \rho_{ac}(T)$, the emergence T^4 dependence at low temperature emphasizes the impact of electron-phonon interaction to resistivity at low temperature since impurity induced resistivity remains independent of temperature within RTA as shown in Eq. (25).

Looking again at Fig. 6, we notice that, resistivity at high-temperature regime, i.e., $T \gg T_{BG}$ changes linearly with T . A clear example can be seen at $T > 50$ K when $n = 2 \times 10^{12}/\text{cm}^2$ and also in the inset of the left panel of Fig. 6 at a larger temperature scale. In order to compare the iterative solution with the results of RTA, we plot in the inset of the left panel of Fig. 6, the total resistivity calculated via $\rho(T) = c(\rho_{\text{imp}} + \rho_{ac}(T))$ with c being constant. The latter has been chosen arbitrarily so as to shift the resistive near the result of self-consistent equations for easy comparison. In addition, we have neglected temperature contribution from impurity since it arises in the second order expansion of the Fermi function. Nevertheless, it is clear that both approaches agree with each other regarding the linear dependence of resistivity at high temperature.

Let us now look at Fig. 7, which plots the thermopower as a function of temperature and carrier density. As is readily seen, thermopower is generally smaller than that in Fig. 3. This may be understood by recalling an inverse relation between D_A and L^{aa} outlined in Eqs. (42), which is also true for L^{ab} . A rather similar could also be derived from the Mott's relation since thermopower depends only on the derivative of σ , which decreases along with D_A . As seen in Fig. 3, S remains uniform for both axes in the presence of electron phonon coupling, which suggests that anisotropic parameters on Eq. (1) does not appear in the ratio of L^{aa} and L^{ab} . The results further demonstrate that variation of thermopower from low to high doping carries signature of electron-phonon interaction, which implies that thermopower might provide a way to deduce deformation potential.

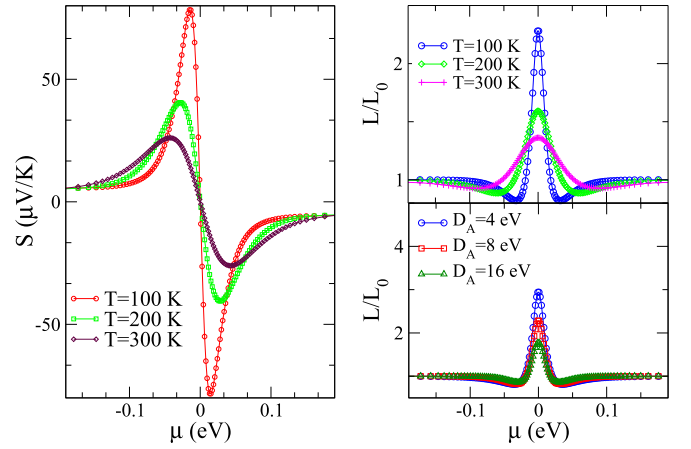


FIG. 7. Left panels: Variation of thermopower as a function of electron carrier density and temperature calculated at $D_A = 8$ eV. Upper right panel shows Lorenz number at $D_A = 8$ eV for different temperature whereas the same is plotted in the lower-right panel at $T = 100$ K for different electron-phonon coupling D_A . Similar to that of Fig. 4, thermopower and Lorenz number for x overlap with that of y axis.

To further identify the signature of electron-phonon interaction, we shall be now looking at the right panels of Fig. 7, which depicts the Lorenz ratio for different electron phonon coupling and temperature. Similar to what is seen in Fig. 4, the Lorenz ratio at high particle or hole doping generally submits to the Wiedemann-Franz's law. This holds from 100 to 300 K and from $D_A = 4$ eV up to 16 eV. A violation to this behavior near the Dirac neutrality point is evident. An increase of Lorenz number as doping decreases could then be understood as a departure from free electron gas at highly doped regime onto interacting electron at low doping. It is interesting to realize, however, that the resonance at small doping tends to diminish or increase when electron-phonon coupling and temperature varies. This signals that in addition to electronic mechanism, phonon-involved process also contributes to such anomaly and makes it more difficult to trace its origin. Nevertheless, the robustness of resonance is a clear testament to an unusual electronic gas at low doping, which is further enhanced by phonon.

Having analyzed charge and heat transport in the presence of phonon, we shall be closing this section with a comment on the Figure of Merit ZT . In Fig. 8 we plot FOM by varying deformation potential D_A and impurity concentration n_i . Following our previous observation that both σ and α varies according to the strength of deformation potential, it is natural to expect that the same also applies for FOM by recalling $ZT = \alpha^2 \sigma / \kappa$. This is indeed appear in Fig. 8 in which ZT becomes minimum when $D_A = 8$ eV. What is interesting is that an increase of impurity concentration helps to suppress thermal conductivity, which eventually yield higher FOM. In the inset of Fig. 8, we observe that a variation of n_i from $5 \times 10^{12}/\text{m}^2$ to $50 \times 10^{12}/\text{m}^2$ at $D_A = 2$ eV amounts to suppressing thermal conductivity and a similar behavior is also seen for $D_A = 8$ eV when n_i increases from $2 \times 10^{12}/\text{m}^2$ to $9 \times 10^{12}/\text{m}^2$. From this observation, we can see that reduction of ZT due to electron-phonon coupling could be compensated

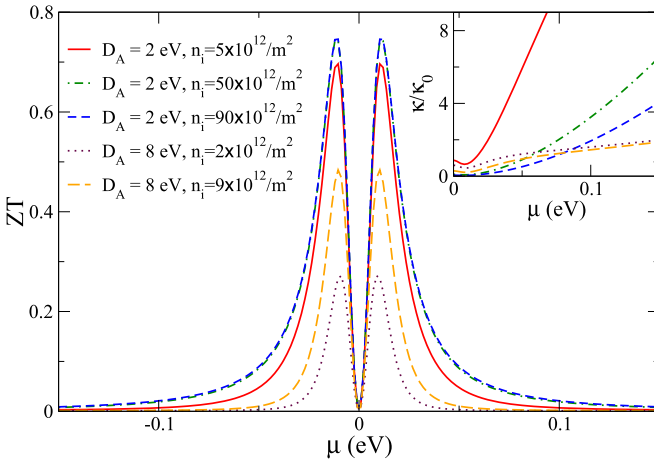


FIG. 8. Figure of merit as a function of electron-phonon coupling D_A and impurity density n_i at $T = 50$ K for both x and y axes. Inset shows the corresponding thermal conductivity measured in $\kappa_0 = eV k_B/h$.

by increasing impurities, which yields a reduction of thermal conductivity. It is important, however, to realize that ZT does not always scale up with impurity density and this can be readily observed above for $D_A = 2$ eV. An increase of n_i from $50 \times 10^{12}/\text{m}^2$ to $90 \times 10^{12}/\text{m}^2$ does not lead to any significant changes since in this regime the conductivity is also suppressed. Since we are not *a priori* aware of the magnitude of electron-phonon coupling, variation of FOM on different substrate is certainly anticipated. A special treatment to induce impurity or even defects on borophene sample might, however, be considered as a viable path to improve FOM and this seems to be necessary when electron-phonon interaction becomes further enhanced in the presence of substrate.

B. Polar optical phonon

Let us now discuss another possible scenario in which the borophene monolayer is supported by substrate with large dielectric constant such as ZrO_2 or HfO_2 . Over the last decades, dielectric materials have been one of the key element of the Si-based transistor as it offers thermodynamic or electrical stability and enables aggressive scaling. In two-dimensional system, e.g., graphene, high dielectric materials have also been actively employed as a substrate since it reduces effect of long-range impurity scattering and thereby improving the mobility. The byproduct generated by remote phonon scattering, however, remains an important issue to be resolved particularly at room temperature since it may limit mobility via a reduction of effective velocity or enhancement of scattering rate. A rather similar problem is also faced by Si-based transistor, which usually suffers from high leakage current. Recent experiment using graphene and polar substrate, however, has suggested that effect of remote phonon scattering could be limited to a certain extent by sandwiching an additional buffer [40].

The role of polar optical phonon scattering in the transport properties of borophene remains largely unexplored. This perhaps has been hampered by experimental realization of suspended borophene and the difficulty to reach chemical

stability when using different substrate other than $\text{Ag}(111)$. Despite the lack of experimental activities, theoretical description on this issue remains of interest since it might be of use once synthesis and characterization are possible. In view of such importance, we shall be devoting this section for the analysis of impact of the electron-phonon scattering when high dielectric material takes a role of substrate. We begin our discussion by expressing the coupling between electron and optical phonon via a Hamiltonian

$$H_{e-op} = \sum_{\mathbf{q}\nu} \mathcal{C}_{\mathbf{q}\nu} (a_{\mathbf{q}} + a_{-\mathbf{q}}^\dagger), \quad (44)$$

where a (a^\dagger) being the annihilation (creation) operator and ν is the polar optical mode,

$$\mathcal{C}_{\mathbf{q}\nu} = \frac{e}{\epsilon_0} \sqrt{\frac{\hbar}{\omega_{so\nu} \gamma_\nu}} \frac{e^{-qd}}{\sqrt{q}},$$

with $\frac{1}{\gamma_\nu} = \frac{\epsilon_0 \omega_{so\nu}^2}{2\pi A} \left[\frac{1}{\epsilon_\infty + \epsilon_{\text{env}}} - \frac{1}{\epsilon_0 + \epsilon_{\text{env}}} \right]$. Here $\hbar\omega_{so}$ being the energy of the surface optical phonon, ϵ_∞ , ϵ_0 refer to high-frequency and zero-frequency dielectric function, respectively. ϵ_{env} is the dielectric constant of environment beyond the polar substrate, which will be taken 1 throughout discussion below and d is the distance separating monolayer borophene and substrate.

By keeping the assumption of weak coupling, which is relevant when boron atom does not strongly coupled with atoms of substrate, we could then express the electron-phonon matrix element within the Born approximation. Carrying out this step with the help of Eq. (44) yields

$$M_{\mathbf{k}\mathbf{k}'}(\mathbf{q}) = \frac{e^2}{\epsilon_0 q \gamma_\nu} (1 + \cos(\theta_{\mathbf{k}} - \theta_{\mathbf{k}'})) e^{-2qd}, \quad (45)$$

where

$$\frac{1}{\gamma_\nu} = \frac{\hbar\omega_{so\nu}}{2\pi A} \left[\frac{1}{\epsilon_\infty + \epsilon_{\text{env}}} - \frac{1}{\epsilon_0 + \epsilon_{\text{env}}} \right].$$

This together with Eq. (36) give transition probability $W_{\mathbf{k}\mathbf{k}'}$ between electron states \mathbf{k} and \mathbf{k}' in the presence of scattering by electron and phonon of polar substrate.

In the numerical evaluation of Boltzmann's equation we shall be keeping the deformation potential D_A at a constant 8 eV. We note that while the choice of D_A was not derived from experimental findings, our calculation suggested that adjustment upon increasing or decreasing D_A only amounts to affecting a quantitative magnitude of transport. In addition to this, the choice of polar substrate presented below has been motivated by the current state of experimental activities on two-dimensional system, which usually employs HfO_2 , ZrO_2 , and SiO_2 as substrates.

Let us now look at Fig. 9, which plots the resistivity of borophene when deposited on top of HfO_2 , ZrO_2 , and SiO_2 substrates. Their optical parameters are described in Table I. At low temperature, $T < 100$ K, we observe that resistivity on all substrates almost coincide whereas beyond $T > 100$ K resistivity tends to diverge and arises nonlinearly with temperature. The former suggests that at low temperature electronic or thermal transport suffers from scattering by either impurity and acoustic phonon only whereas the latter at high

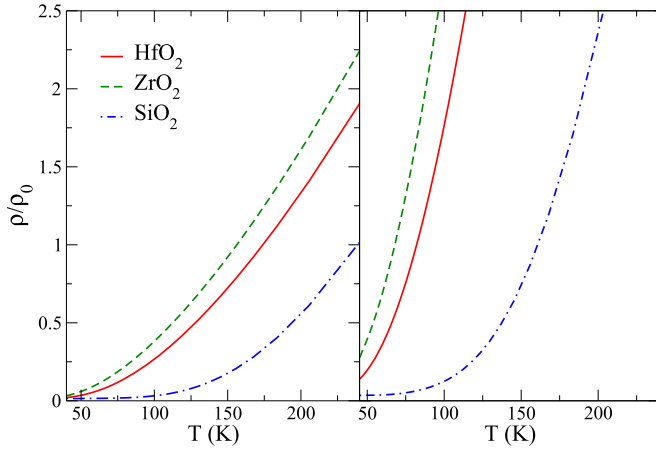


FIG. 9. Temperature-dependent resistivity of borophene on top of three different substrates at constant carrier density $n = 1 \times 10^{12}/\text{cm}^2$ and $d = 2$ nm. Left and right panels describe resistivity along the x and y axes, respectively.

temperature, $T > 100$ K, transport is also affected by scattering due to remote optical phonon, which subsequently yields a higher resistivity. As expected, the resistivity on x axis remains smaller than that on y . This suggests that the inclusion of polar substrate does not affect the crystal symmetry, which underlies anisotropic Dirac cone.

Variation of resistivity on different substrate tells us further that ρ depends not only on the energy of optical phonon $\hbar\omega_{so}$ but also on the magnitude of dielectric constant ϵ particularly that with low frequency. At first glance, it is natural to expect that the use of substrate with small dielectric constant seems to give a positive feedback on transport than that with large dielectric constant. We note that this is indeed true when we are interested for transport at large temperature, i.e., $T \geq 50$ K, as presented above, but does not necessarily applicable at low temperature. The latter case has been discussed thoroughly for graphene in [42], which points out that at low temperature, high dielectric constants turns out to yield a better conductivity. Nevertheless, since real implementation of borophene is expected to be carried out near room temperature, we should expect that substrate with small dielectric constant such as SiO_2 should provide the most optimal transport. Further comments on this aspect will be outlined below.

Under certain circumstance that the suitable substrates consists of a large dielectric constant, it is then interesting to find other viable route to suppress the impact of scattering by polar optical phonon. As pointed out above, another possible path is to vary the distance between the substrate and the borophene by introducing the buffer layer. In order to examine

TABLE I. Surface polar phonon energies and dielectric constants for HfO_2 , SiO_2 and ZrO_2 [41,42].

	ϵ_0	ϵ_∞	$\hbar\omega_{\text{SO}_1}$ (meV)	$\hbar\omega_{\text{SO}_2}$ (meV)
HfO_2	22	5.03	25.6	54.2
SiO_2	3.9	2.5	58.9	156.4
ZrO_2	24	4	16.67	70.8

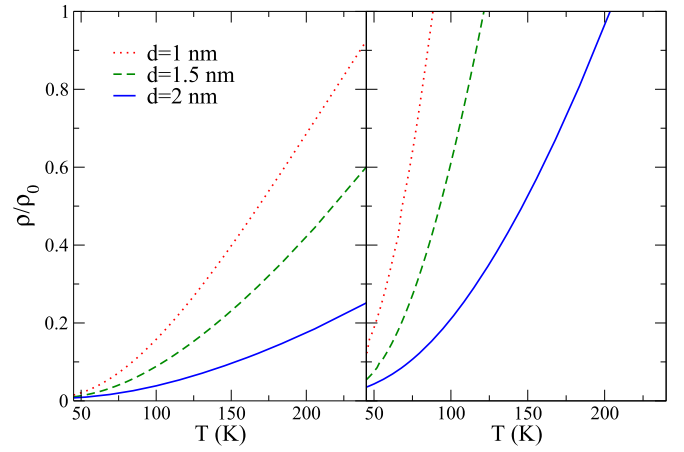


FIG. 10. At carrier density $n = 2 \times 10^{12}/\text{cm}^2$, the lines correspond to temperature-dependent resistivity of HfO_2 as a function of temperature and for different magnitude of d , distance between polar substrate and monolayer borophene.

this, we plot in Fig. 10 the temperature dependent-resistivity for various distance d . As is readily seen, the resistivity indeed decays proportionally to e^{-2qd} when d increases such that at large spacing, i.e., $d = 2$ nm, the resistivity becomes smaller than that for $d = 1$ nm. Our results, however, do not suggest for a meaningful effect on resistivity when d further increases beyond that is indicated in Fig. 10.

In order to benchmark the impact of internal and external perturbation, we plot in the left panel of Fig. 11, the mobility of borophene in the y direction for various conditions, i.e., intrinsic (with long range impurity only), nonpolar (with acoustic phonon) and after using polar substrates. As expected, borophene has very large mobility from low to high temperature in the absence of phonon but it significantly

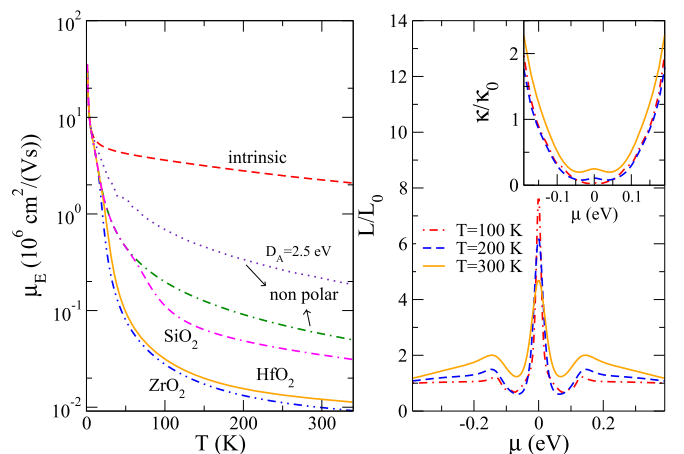


FIG. 11. Left panel: Temperature dependence of the mobility μ_E on the y axis with polar or nonpolar substrate calculated at carrier density $2 \times 10^{11}/\text{cm}^2$. Except for dotted line, which is calculated at $D_A = 2.5$ eV, other lines are obtained at $D_A = 8$ eV. Right panels shows Lorenz number of borophene on top of ZrO_2 for different carrier number from $T = 100$ K up to $T = 300$ K. Within the same parameters, inset shows variation of the thermal conductivity. In the right panels, L and κ for x overlap with that of y .

TABLE II. Direction-dependent mobility of borophene on top of HfO₂, SiO₂ and ZrO₂ at $T = 340$ K.

	$\mu_{xx}(10^4 \text{cm}^2/\text{Vs})$	$\mu_{yy}(10^4 \text{cm}^2/\text{Vs})$
HfO ₂	7.37	1.12
SiO ₂	8.68	3.12
ZrO ₂	7.62	0.92

decreases, already when nonpolar substrate is used. This can be realized at $T = 340$ K in which mobility along the y direction is suppressed down to $1.6 \times 10^5 \text{ cm}^2/\text{Vs}$ for $D_A = 2.5$ eV and further to $5 \times 10^4 \text{ cm}^2/\text{Vs}$ for $D_A = 8$ eV. It is interesting to note that the former resembles the result outlined in [31] in the order of $7.72 \times 10^5 \text{ cm}^2/\text{Vs}$, which is derived within DFT and deformation potential theory. When borophene is deposited on top of polar substrate, we observe further reduction of mobility. At $T = 340$ K, the mobility decreases to $9.2 \times 10^3 \text{ cm}^2/\text{Vs}$ for ZrO₂ substrate whereas for SiO₂ the mobility improves up to the order of $3 \times 10^4 \text{ cm}^2/\text{Vs}$. We note in passing that a similar trend is also true for x direction but with a larger magnitude of mobility. A quantitative comparison of mobility between x and y direction on various substrate is shown in Table II. It can then be concluded that borophene on top of SiO₂ provides reasonable value of mobility and a small discrepancy between x and y axes.

Let us move on further to examine the behavior of electronic gas with the attention paid to the influence of additional scattering from remote phonon. Figure 11 plots the Lorenz ratio of borophene on top of ZrO₂ as a function of doping and temperature whereas the inset displays the corresponding thermal conductivity.

At large doping, we readily observe an overlap of κ , which implies for L that becomes equivalent with the Lorenz number L_0 . This is a clear signature of metallic gas consisting of ensemble of particles moving freely on a lattice. In contrast to previous observation, cf. Fig. 4 and Fig. 7, in which $L = L_0$ enters at $\mu = 0.1$ eV, $L = L_0$ in the present of polar optical phonon appears at relatively higher doping, i.e., $\mu = 0.2$ eV. This is understandable by realizing that the use of polar material further enhances electron-phonon interaction and such impact might be suppressed by increasing charge carrier.

At low density $n < 10^{12} /\text{cm}^2$, the Lorenz ratio consists of resonance, which can be seen as a counterpart of the small peak in the thermal conductivity. What distinguishes the present result with those in Fig. 4 is the dependence of L on temperature even at the charge neutrality point. While this might suggest for an enhancement of interaction, it is important to be aware of that its origin does not exclusively correspond to electron mechanism. Similar to the previous case with acoustic phonon, electron scattering at low doping is also interfered by electron-phonon process. This argument could be justified by looking back to the right panel of Fig. 7 showing variation of L together with temperature and D_A . In addition, Eqs. (41) and (43) also explain that scattering lifetime depends on the temperature and its impact is further enhanced with the presence of optical phonon. From experimental point of view, the above observation suggests that

resonance near charge neutrality point for borophene on top of polar optical phonon should be treated with caution. This is necessary since its origin does not directly correspond to electron mechanism contributing to Dirac point but might arise via electron-phonon interaction.

We conclude by mentioning that important signatures of transport of borophene such as anisotropy in resistivity or interacting electronic gas at low density are generally unaffected by polar substrate. Qualitatively, they are not too much different from that in the absence of remote phonon scattering. Quantitatively, however, we find a reduction of mobility, an increase of resistivity as temperature goes up approaching a room temperature. We have demonstrated that near room temperature, the use of substrate with small dielectric constant and buffer layer amounts to alleviating the impact of remote phonon scattering.

V. PHONON DRAG

Interaction between electron and substrate acoustic phonon could induce additional mechanism known as phonon drag that contributes to a thermopower. In the presence of temperature gradient, a flux of phonon may flow from the hot side to the other cold side of the sample, carries electron with it and thereby generating an electric field. The effect of phonon drag is therefore expected to increase the thermopower. In light of the possibility of drag effect, interpretation of the thermopower data is generally complicated and should be undertaken carefully. There are two mechanisms involved in generating a thermopower consisting of the usual diffusive and the other being phonon drag. The ability to distinguish the impact of one mechanism from the other is necessary to be able to comprehensively understand how charge or heat is transported in borophene.

The drag mechanism is different from the phonon contribution discussed in the previous section since for drag effect to occur, phonon can not be treated by directly assuming the occupation in thermal equilibrium, i.e., $n_{\mathbf{q}} = n_{\mathbf{q}}^0$. This follows from an argument that phonon as well as electron shall be deviating from their equilibrium state, which is triggered by the temperature difference between two sides of a sample. Indeed, such situation might be expected to arise in the realistic scenario of low field transport. Hence, it is useful to elucidate the condition under which the phonon drag might contribute to thermal properties or to find a way to distinguish it from the usual equilibrium phonon. It is interesting to note, however, that from a number of thermopower measurements in graphene at low and high temperature, there is no strong evidence suggesting a positive effect of phonon drag on thermopower. Nevertheless, examining the possibility of drag thermopower in borophene might still be interesting particularly due to an unusual anisotropy of the band structure.

Our discussion below will therefore be aimed at investigating the role of anisotropy on the drag thermopower and the analysis shall be based on the level of the relaxation time approximation. As we have demonstrated in the previous sections, RTA, albeit its simplistic treatment of scattering on the Fermi surface, is still, nonetheless, a faithful approach to derive a transport coefficient particularly a thermopower. Its main advantage has been that it facilitates an analytical

simplification of the drag coefficient yielding a better insight on the role of anisotropic Fermi velocities.

When phonon drag is accounted for, the thermopower consists of two different mechanisms; the diffusive and the phonon drag. They are linearly additive such that the total thermopower S^T can be expressed as $S^T = S + S^g$ where $S_{ii}^g = \frac{L_{ii}^g}{L_{ii}}$ denotes the drag coefficient along the i direction. As in the case of diffusive transport, the contribution to drag effect might involve either acoustic or optical branch depending on the temperature of experiment and the choice of substrate. In this section, we shall be discussing the impact of acoustic phonon on drag coefficient.

The formulation of the drag coefficient requires a simultaneous solution of Boltzmann's equation for both electron and phonon, i.e., Eqs. (12) and (13). The solution of such coupled equations is demanding but it can, however, be simplified by assuming that both electron or phonon distributions are close to equilibrium so much so that they can be linearly expanded around their local equilibrium distribution [43,44]. In this way, the contribution to charge current comes not only from the usual drift process but also from phonon drag, which takes the form of

$$L_{ii}^g = \frac{e}{k_B T^2} \sum_{\mathbf{k}\mathbf{k}'\mathbf{q},\lambda\lambda'} \chi_{ii,\lambda\lambda'}(\mathbf{k}, \mathbf{k}', \mathbf{q}),$$

$$\chi_{ii,\lambda\lambda'}(\mathbf{k}, \mathbf{k}', \mathbf{q}) = \hbar\omega_{\mathbf{q}} f_0(\epsilon_{\mathbf{k},\lambda})(1 - f_0(\epsilon_{\mathbf{k}',\lambda'})) W_{\mathbf{k}\lambda,\mathbf{k}'\lambda'} \tau_{ph}$$

$$\times \mathbf{v}_{ph,i} \cdot (\mathbf{v}_{\mathbf{k}\lambda,i} \tau_{\mathbf{k}\lambda} - \mathbf{v}_{\mathbf{k}',\lambda',i} \tau_{\mathbf{k}'\lambda'}), \quad (46)$$

where $W_{\mathbf{k}\lambda,\mathbf{k}'\lambda'}$ is the transition rate of electron from state $\mathbf{k}\lambda$ onto $\mathbf{k}'\lambda'$ by absorbing phonon as expressed in Eq. (36). Subscript i denotes x or y direction, e is the electron charge, and $\tau_{ph} = \Lambda_{ph}/v_s$ for Λ_{ph} being the mean-free path of phonon, which shall be assumed throughout to be independent of \mathbf{q} . $\omega_{\mathbf{q}} = v_s|\mathbf{q}|$, $v_{ph} = v_s\mathbf{q}/|\mathbf{q}|$ denotes the phonon group velocity with v_s being the sound velocity in borophene. $\tau_{\mathbf{k}}$ is the momentum-dependent relaxation-time of electron, which shall be considered only on certain values of $E_{\mathbf{k}}$, near the Fermi surface.

In order to evaluate the drag contribution according to Eq. (46), we shall be working with the modified Hamiltonian of Eq. (4). Since variables in Eq. (4) have been switched onto p_x and p_y following the definition of Eq. (3), it is also necessary to adjust the wave vectors q_x and q_y using new variables r_x and r_y as follows:

$$r_x = \sqrt{\frac{v_x}{v_y}} q_x,$$

$$r_y = \sqrt{\frac{v_y}{v_x}} q_y. \quad (47)$$

Substitution of Eqs. (3), (5), and (47) onto Eq. (46) yields drag coefficient along the x direction reads

$$L_{xx}^g = -\frac{2\pi}{\hbar} \frac{e\Lambda_{ph}}{k_B T^2} \sqrt{\frac{v_y}{v_x}} \sum_{\mathbf{q}} (\hbar\omega_{\mathbf{q}})^2 \int dp |C_{\mathbf{p}\mathbf{q}}|^2$$

$$\times \frac{n_{\mathbf{q}}^0}{\sqrt{4p^2 r^2 - (\zeta^2 - r^2 - 2p\zeta)^2}} \frac{\tau_{\mathbf{p}_F} r_x}{qr}$$

$$\times f_0(\epsilon_{\mathbf{p}})(1 - f_0(\epsilon_{\mathbf{p}} + \hbar\omega_{\mathbf{q}})) H_{xx}(\mathbf{r}, \mathbf{p}), \quad (48)$$

where $\zeta = \eta\hbar v_o r_y$, $r = \sqrt{r_x^2 + r_y^2}$, and other variables are defined as follows:

$$|C_{\mathbf{p}\mathbf{q}}|^2 = \frac{D_A^2}{2A\rho_B v_s^2} (1 + \cos(\theta_{\mathbf{p}} - \theta_{\mathbf{q}})),$$

$$H_{xx}(\mathbf{r}, \mathbf{p}) = (\zeta^2 - r^2 - 2p\zeta)(\zeta - 2p) - 2pr r_x. \quad (49)$$

Similar steps yields the drag coefficient along the y direction,

$$L_{yy}^g = -\frac{2\pi}{\hbar} \frac{e\Lambda_{ph}}{k_B T^2} \sqrt{\frac{v_x}{v_y}} \sum_{\mathbf{q}} (\hbar\omega_{\mathbf{q}})^2 \int dp |C_{\mathbf{p}\mathbf{q}}|^2$$

$$\times \frac{n_{\mathbf{q}}^0}{\sqrt{4p^2 r^2 - (\zeta^2 - r^2 - 2p\zeta)^2}} \frac{\tau_{\mathbf{p}_F} r_y}{qr}$$

$$\times f_0(\epsilon_{\mathbf{p}})(1 - f_0(\epsilon_{\mathbf{p}} + \hbar\omega_{\mathbf{q}})) H_{yy}(\mathbf{r}, \mathbf{p}), \quad (50)$$

with

$$H_{yy}(\mathbf{r}, \mathbf{p}) = (\zeta - 2p)\sqrt{4p^2 r^2 - (\zeta^2 - r^2 - 2p\zeta)^2} - 2pr r_y.$$

To get a better perspective on the above equations, we can set $\zeta = 0$, which amounts to setting the tilted velocity $v_t = 0$. Integral over variable p can be worked out by considering a system at low temperature, which allows one to set $f_0(\epsilon_{\mathbf{p}}) - f_0(\epsilon_{\mathbf{p}} + \hbar\omega_{\mathbf{q}}) \approx \hbar\omega_{\mathbf{q}}(n_{\mathbf{q}}^0 + 1)\delta(\epsilon_{\mathbf{p}} - \epsilon_F)$. In this way, the drag coefficient becomes

$$L_{xx}^g = -\frac{2\pi}{\hbar} \frac{e\Lambda_{ph}}{k_B T^2} \frac{D_A^2}{A\rho_B \hbar^2 v_s^3 v_F} \sqrt{\frac{v_y}{v_x}} \sum_{\mathbf{q}} (\hbar\omega_{\mathbf{q}})^4$$

$$\times n_{\mathbf{q}}^0 (n_{\mathbf{q}}^0 + 1) \frac{\tau_{\mathbf{p}_F} r_x^2}{qr} \sqrt{1 - \frac{\gamma^2}{4\epsilon_F^2}},$$

$$L_{yy}^g = -\frac{2\pi}{\hbar} \frac{e\Lambda_{ph}}{k_B T^2} \frac{D_A^2}{A\rho_B \hbar^2 v_s^3 v_F} \sqrt{\frac{v_x}{v_y}} \sum_{\mathbf{q}} (\hbar\omega_{\mathbf{q}})^4$$

$$\times n_{\mathbf{q}}^0 (n_{\mathbf{q}}^0 + 1) \frac{\tau_{\mathbf{p}_F} r_y^2}{qr} \sqrt{1 - \frac{\gamma^2}{4\epsilon_F^2}}, \quad (51)$$

where $\gamma = \hbar v_F r$. In order to proceed further, we notice that the above equations depend on q and r , with the latter carries nonuniform coefficients related to ratio of velocities. At low temperature, we set $q \sim r$ by following the observation from numerical result that the discrepancy induced by velocities is minimal, i.e., drag coefficient along x or y is almost indistinguishable. This approximation amounts to neglecting integral over the angle between wave vector \mathbf{q} , which also deteriorates numerical accuracy. Further, by taking $q \rightarrow 0$ and $\sqrt{1 - \frac{\gamma^2}{4\epsilon_F^2}} \rightarrow 1$ the integral over q can then be carried out in a straightforward manner. To derive the drag thermopower, we shall be requiring that the conductivity along $\epsilon_{\mathbf{p}} \sim \epsilon_F$ at low temperature takes the form of $\sigma_{xx} = \frac{e^2 v_x^2}{\hbar} \frac{\epsilon_F \tau_{\mathbf{p}_F} I_{xx}}{v_y^2 \pi}$, and $\sigma_{yy} = \frac{e^2 v_x^2}{\hbar} \frac{\epsilon_F \tau_{\mathbf{p}_F} I_{yy}}{\pi}$, where $I_{xx} = \int d\theta \frac{1}{z^2(\theta)} \frac{\cos^2(\theta)}{l_0^2(\theta)}$, and $I_{yy} = \int d\theta \frac{1}{z^2(\theta)} \frac{\sin^2(\theta)}{l_0^2(\theta)}$. By combining the above expression with L_{xx}^g

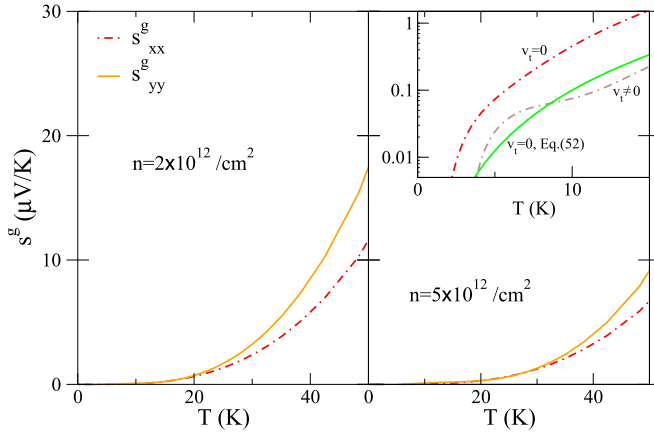


FIG. 12. Drag thermopower of 8-*Pmmn* borophene for two carrier density $n = 2 \times 10^{12}/\text{cm}^2$ (left panel) and $n = 5 \times 10^{12}/\text{cm}^2$ (right panel). Dashed-dotted (solid) lines correspond to thermopower for x (y) axis. The inset in the right panel on the log-scale depicts drag thermopower with or without v_t and also numerical evaluation of Eq. (52).

and L_{yy}^g , we find the drag thermopower as

$$s_{xx}^g = \sqrt{\frac{v_y^5 D_A^2 \Lambda_{ph} k_B^4 T^3 4! \zeta(4)}{v_x^5 e \rho_B \epsilon_F \hbar^3 v_s^4 v_F I_{xx}}}, \quad (52)$$

$$s_{yy}^g = \sqrt{\frac{v_x^5 D_A^2 \Lambda_{ph} k_B^4 T^3 4! \zeta(4)}{v_y^5 e \rho_B \epsilon_F \hbar^3 v_s^4 v_F I_{yy}}}.$$

The drag thermopower depends explicitly on the velocity and angle integrals I_{xx} and I_{yy} , which distinguishes s_{xx}^g from s_{yy}^g . They also exhibit T^3 power law, much similar to what is seen in graphene.

In order to get a complete view of the drag effect of borophene with nonzero v_t , we need to evaluate Eqs. (48) and (50). In the numerical implementation, we employed $D_A = 8$ eV, a constant $\tau_{pf} = 10^{-12}$ s and $\Lambda_{ph} = 10^{-8}$ m. The latter gives constant phonon relaxation time at the order of 10^{-14} s. Other parameters follow those outlined in Sec. IV A.

Figure 12 draws the drag thermopower for $n = 2 \times 10^{12}/\text{cm}^2$ and $n = 5 \times 10^{12}/\text{cm}^2$ in the left and right panels, respectively. As is readily realized, at low temperature, $T < 10$ K, the drag coefficient is negligible, which implies that contribution to thermopower is expected to come mainly from diffusive process. This, however, changes as temperature goes up beyond $T = 10$ K in which the drag coefficient sets in and increases nonlinearly. From the inset in the right panel of Fig. 12 we learn that for nonzero v_t , the drag coefficient also changes according to T^3 with temperature but becomes slightly larger than the analytical result of Eq. (52). Such behavior appears on both x and y axes. When carrier density gets larger, one observes a suppression of drag coefficient, which implies for the reduction of the phonon drift as a consequence of frequent scattering of phonons by the carrier.

While temperature dependence of the drag coefficient with and without tilted velocity seems to follow that of graphene, an important feature of phonon drag of borophene is its dependence on x and y axes. This can be seen already from

Eq. (52), which consists of pre-factors of the ratio of velocities together with angle integrals I_{xx} and I_{yy} . In the case of nonzero tilted velocity, anisotropy seems to arise not only from the pre-factors alone but also from parameters r_x or r_y , which carry wave vector q . In addition to this, the discrepancy between drag effect with zero v_t and that with finite v_t is in their magnitude, in which the latter is smaller than the former. The main reason for this has been the reduction of the conductivity for $v_t = 0$ leading to a larger drag coefficient. Thus by following the above argument, it is natural to anticipate that drag effect in 8-*Pmmn* borophene might be identified more straightforwardly via thermopower measurement. The absence of anisotropy in the thermopower links to diffusive process whereas the emergence of anisotropic thermopower might be considered as a smoking gun of the drag effect.

VI. ENERGY RELAXATION

Another interesting aspect, which has continuously drawn considerable interest is the mechanism of transfer of energy between hot carriers and the surrounding environment. Under the influence of electric field, carrier gains energy, heats up to a temperature that is higher than their environment before finally giving off the excess of energy. At relatively low temperature, hot carriers of borophene on top of substrate are expected to cool down by releasing energy via acoustic phonon emission whereas at high temperature a similar process should involve an emission of optical phonon. Heat transport experiments such as $p - n$ junction photocurrent or noise thermometry have routinely been used as a means to trace hot electrons in graphene and offer an indirect route to probe temperature of electron, i.e., via Johnson noise [45,46]. Perhaps, one of the most important quantities that can be derived from these experiments is the electron-phonon coupling, i.e., deformation potential D_A in the case of the acoustic phonon. A comprehensive understanding of dynamics of hot carriers under influence of vibrating lattice is thus interesting not only from fundamental point of view but also for the future realization of borophene based electronics or sensors, which demands an efficient exchange of energy.

In order to determine the average rate at which carrier loses its energy to either acoustic or optical mode, we shall be looking at the rate of change of the number of phonon $\frac{dn_q}{dt}$ due to emission by carrier. By summing this with the available phonon, which has the same wave vector \mathbf{q} , the power loss could be expressed as

$$P = -\frac{1}{n} \sum_{\mathbf{q}} \hbar \omega_{\mathbf{q}} \frac{dn_{\mathbf{q}}}{dt} \quad (53)$$

where n is the number of electrons and

$$\frac{dn_{\mathbf{q}}}{dt} = \frac{2\pi}{\hbar} \sum_{\mathbf{k}\lambda\lambda'} |M_{\mathbf{k}\mathbf{k}'}(\mathbf{q})|^2 \delta_{\mathbf{k}',\mathbf{k}+\mathbf{q}} \delta(\epsilon_{\mathbf{k},\lambda} - \epsilon_{\mathbf{k}',\lambda'} + \hbar\omega_{\mathbf{q}}) \times [(n_{\mathbf{q}} + 1)f_{\mathbf{k}'\lambda'}(1 - f_{\mathbf{k}\lambda}) - n_{\mathbf{q}}f_{\mathbf{k}\lambda}(1 - f_{\mathbf{k}'\lambda'})]. \quad (54)$$

A. Acoustic phonon

When electrons interact with longitudinal acoustic phonon, the phonon dispersion will be taken linear as $\omega_{\mathbf{q}} = v_s \mathbf{q}$ whereas the electron-phonon coupling $M_{\mathbf{k}\mathbf{k}'}$ follows Eq. (40).

In order to evaluate $F(T)$, we shall be implementing the same strategy outlined in the previous section, i.e., working with variables p defined in (3) and r in Eq. (47). By expressing P in the form of

$$P = F(T_e) - F(T_L), \quad (55)$$

and carrying out the above steps yields

$$F(T) = \frac{1}{n\hbar^2} \sum_{\mathbf{q}} (\hbar\omega_{\mathbf{q}})^2 \sum_{\mathbf{p}} |C_{\mathbf{p}\mathbf{q}}|^2 \times \frac{\sqrt{\zeta^2 - 2\zeta p + p^2}}{\sqrt{4p^2 r^2 - (\zeta^2 - r^2 - 2\zeta p)^2}} \times (f_0(\epsilon_{\mathbf{p}}) - f_0(\epsilon_{\mathbf{p}} + \hbar\omega_{\mathbf{q}})) n_{\mathbf{q}}^0 / v_F, \quad (56)$$

$\zeta = \eta\hbar v_o r_y$, $r = \sqrt{r_x^2 + r_y^2}$, and $|C_{\mathbf{p}\mathbf{q}}|$ is defined in Eq. (49). Following the previous analysis, we can get a better perspective on the function $F(T)$ by putting off the tilted velocity $\zeta = 0$. Direct implementation yields

$$F(T) = -\frac{D_A^2}{n\rho_B v_s^2 \hbar^4 v_F^3} \int dq (\hbar\omega_{\mathbf{q}})^2 \int d\epsilon_{\mathbf{p}} \sqrt{\epsilon_{\mathbf{p}}^2 - \gamma^2 n_{\mathbf{q}}^0} \times (f_0(\epsilon_{\mathbf{p}}) - f_0(\epsilon_{\mathbf{p}} + \hbar\omega_{\mathbf{q}})). \quad (57)$$

The above expression can be further simplified by working at low temperature, which allows for the use of the previous relation $f_0(\epsilon_{\mathbf{p}}) - f_0(\epsilon_{\mathbf{p}} + \hbar\omega_{\mathbf{q}}) \approx \hbar\omega_{\mathbf{q}} \delta(\epsilon_{\mathbf{p}} - \epsilon_F)$. By substituting this relation onto Eq. (57) and setting $\mathbf{q} \rightarrow 0$ yields a closed form as

$$F(T) \simeq -\frac{D_A^2 \epsilon_F (k_B T)^4 3! \zeta(4)}{n\rho_B \hbar^5 v_s^3 v_F^3}, \quad (58)$$

which corresponds to expression of that of graphene, i.e., $F(T)$ consisting of T^4 dependence [47]. Note that in deriving the above equations we have made a similar approximation used in the previous section, namely $q \sim r$, which is applicable at low temperature.

Equation (58) suggests that in the absence of tilted-velocity the direction-dependent Fermi velocity v_x and v_y does not play a role in determining the average loss of energy. Consequently, transfer of energy between electron and acoustic phonon should proceed very much the same as in that of graphene. It could also be understood by recalling that in the absence of tilted velocity, the low-energy dispersion becomes similar with that of graphene but with different gradient. In order to examine the way energy is passed on to lattice with nonzero v_t , we shall be integrating Eq. (57) numerically. Without loss of generality, we shall be assuming in what follows that the temperature of substrate lattice is far lower than those of carrier, i.e., $T_L=0$.

Figure 13 plots the average loss of electron energy as a function of carrier density n and electron temperature, which is calculated at $D_A = 8$ eV. Other parameters, follows that outlined in the previous sections. As expected, the power loss P consists of the T^4 dependence much the same as graphene with zero v_t . The inclusion of tilted velocity amounts to suppressing the power loss, which is easily seen in the inset of Fig. 13.

Following the analytical formula, we learn that P depends on charge density as $n^{-1/2}$, which implies that an increase

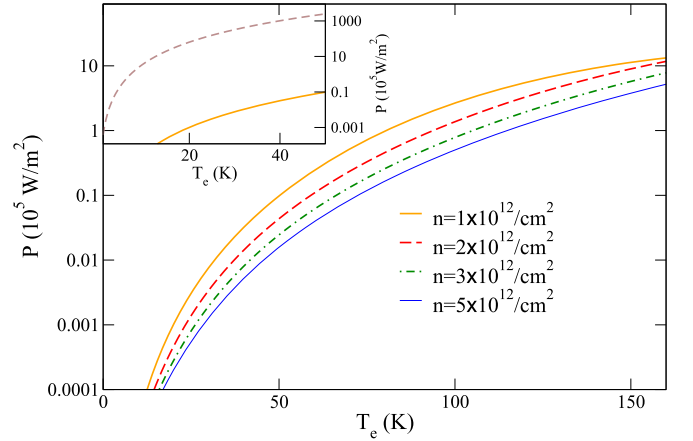


FIG. 13. Electron power loss (on a log scale) as a function of carrier density n and temperature T with constant impurity concentration. The same is also shown in the inset for $v_t = 0$ (dashed lines) and $v_t = 0.32v_{F0}$ (solid lines) at $n = 1 \times 10^{12}/\text{cm}^2$.

number of carrier is followed by a decrease of energy transfer. This relations seems to hold in a full solution of Eq. (59) from low up to 150 K as shown in Fig. 13. A clear example can be seen at $T = 150$ K in which a change of $n = 1 \times 10^{12}/\text{cm}^2$ up to $n = 5 \times 10^{12}/\text{cm}^2$, leads to a suppression of P from 1.3×10^6 W/m² down to 4.5×10^5 W/m².

On top of this, power loss could also provide an estimate of the amount of time required by electron to reach equilibrium after releasing energy. This is achieved by means of $\tau = c_e (dP/dT_e)^{-1}$, with c_e being the specific heat of electron. By concentrating at carrier density $n = 5 \times 10^{12}/\text{cm}^2$, we learn, by using analytical formula with zero v_t that it will require 0.2 fs to lose heat when electron temperature at $T_e = 1$ K whereas at $T_e = 100$ K, requires 0.05 fs. This tells that the cooling time is faster at higher temperature than at low temperature. We can understand this by realizing that there are a large amount of phonon to absorb energy emission of hot carrier at high temperature, which in contrast to a smaller number of phonon at low temperature. We note, however, that the above approximation via RTA usually overestimates cooling time and this might even more pronounced in the present case following a simplification of integral employed above. To conclude this section, it is worth mentioning that $F(T)$ changes quadratically with D_A signifies the sensitivity of power loss to the strength of electron-phonon coupling. It clearly suggests that power loss data are not only necessary for application but also become a useful source when the magnitude of deformation potential is in demand.

B. Polar optical phonon

Having observed energy transfer between carrier and acoustic phonon, let us now briefly look at the cooling mechanism of electron with polar optical phonon. To examine this, we shall be again evaluating Eqs. (53) and (54). By following

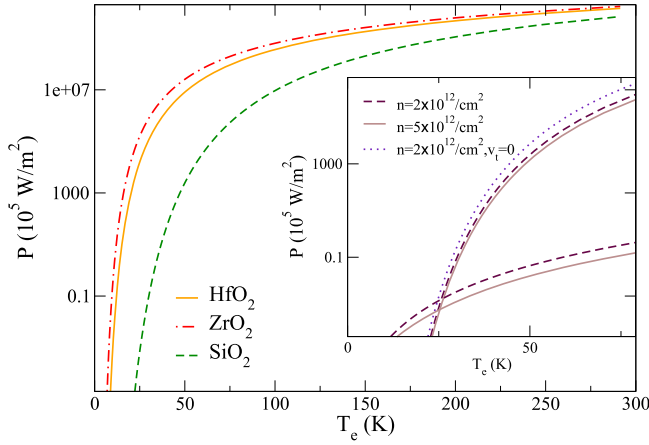


FIG. 14. Electron power loss of borophene on top of three different polar substrates calculated as a function of temperature but at constant density $n = 2 \times 10^{12}/\text{cm}^2$. Inset shows power loss with acoustic phonon and surface optical phonon for SiO_2 calculated at two different carrier density. In addition, the dotted line corresponds to the power loss with zero tilted velocity.

the same steps as outlined before, we readily arrive at

$$F(T) = \frac{1}{n\hbar^2} \sum_{\mathbf{q}_v} \sum_{\mathbf{p}} |C_{\mathbf{q}_v}|^2 \frac{\sqrt{\zeta^2 - 2\zeta p + p^2}}{\sqrt{4p^2 r^2 - (\zeta^2 - r^2 - 2\zeta p)^2}} \times (f_0(\epsilon_{\mathbf{p}}) - f_0(\epsilon_{\mathbf{p}} + \hbar\omega_{SO_v})) n_{\mathbf{q}}^0, \quad (59)$$

$$\zeta = \eta \hbar v_o r_y, \quad r = \sqrt{r_x^2 + r_y^2}, \quad \text{and}$$

$$|C_{\mathbf{q}_v}|^2 = \hbar\omega_{SO_v} \frac{e^2}{q\gamma_v} (1 + \cos(\theta_{\mathbf{p}} - \theta_{\mathbf{q}})) e^{-2qd}.$$

By using different substrates, we plot the numerical result of Eq. (59) in Fig. 14 as a function of electron temperature with constant density $2 \times 10^{12}/\text{cm}^2$ and $d = 1$ nm. As is readily seen, the power loss increases nonlinearly along with temperature but then decreases as carrier density increases similar to what is seen previously in Fig. 13. The largest power loss turns onto maximum for small $\hbar\omega_{SO_v}$, i.e., HfO_2 or ZrO_2 but becomes minimal for SiO_2 , which has a large phonon energy resembling what is seen in bilayer graphene [48]. This implies that on a substrate with larger dielectric constant and lower phonon energy, probability of energy exchange is higher due to large number of available phonon.

Upon comparison with power loss involving only acoustic phonon (see inset of Fig. 14), we readily realize that the onset of energy transfer for polar optical is approximately two times higher than that induced by acoustic phonon. As previously pointed out, such behavior is expected since polar optical substrate consists of energetic phonon, which mainly interacts with electron of higher energy. The emergence of energy transfer at $T = 24$ K thus signifies that optical phonon remains important far below the room temperature. Another important point is that around $T = 25 - 27$ K, there is a crossover from the acoustic to optical phonon dominated process that contributes to cooling power. As is shown above, the temperature at which the optical phonon takes over the acoustic process is determined by a number of factors such as

carrier density and also tilted velocity. The absence of the latter is found to yield higher cooling power at high temperature similar to what is observed previously in Fig. 13. The results thus hint at the advantage of polar material as a substrate namely that it provides additional channel for relaxation of momentum and energy at higher temperature in addition to that is given by acoustic phonon.

VII. SUMMARY AND CONCLUSIONS

We have discussed charge and heat transport of monolayer borophene in the presence of impurity and lattice vibration, i.e., acoustic and optical phonon. With the view of describing a realistic system consisting of monolayer borophene deposited on top of substrate, we focus on transport induced by weak external field or thermal gradient in the presence of impurity or electron-phonon coupling. To derive transport coefficients, we have employed the Boltzmann's transport equations, which is solved self-consistently via direction-dependent mean-free path so as to capture all possible scattering arises on the anisotropic Fermi surface. We complement and analyze the self-consistent results by including the analytical formulation derived within the relaxation time approximation.

Our discussion starts with transport in the absence of phonon. It is shown that charge transport depends on the direction of measurement which reflects the anisotropy of the Fermi surface. This is evident in conductivity, resistivity, mobility, and thermal conductivity but it is absent in the thermopower. The conductivity of borophene with long-range impurity is found to obey quadratic power law on a number of carriers similar to that of graphene. On the basis of thermal conductivity and Lorenz ratio, we further establish that variation of large to small doping amounts to inducing a crossover from Drude metallic behavior to an interacting like electron gas.

In order to get a more sensible description of supported borophene, we move on to incorporate electron-phonon coupling. We consider two additional contributions that might affect charge and thermal transport namely acoustic and polar optical phonon while neglecting a high-temperature optical phonon. With nonpolar substrate, we concentrate on the role of acoustic phonon whose influence is non-negligible at low up to a high temperature. By incorporating both impurity and acoustic phonon, we find that below the T_{BG} , relaxation time and subsequently resistivity varies according to T^4 whereas above T_{BG} they change linearly with temperature. Similar to the case without phonon, charge transport coefficient reflects anisotropy of Fermi surface through its dependence on the Fermi velocities on x and y axes.

When monolayer borophene sits on top of polar substrate, we analyze the impact of remote optical phonon on charge transport particularly at high temperature. By comparing transport on three different substrates, we demonstrate that remote phonon increases scattering rate and this becomes further noticeable in the resistivity near room temperature. We find that mobility of the supported borophene decreases almost two order of magnitude compare to that in the suspended borophene. We then examine the possibility of reducing the impact of remote phonon by changing the distance between

substrate and borophene. Our results indeed shows that sandwiching a buffer layer between polar substrate and borophene helps to reduce impact of remote phonon scattering, which is testified by a reduction of resistivity. Our results further suggest that violation of Wiedemann-Franz's law at low doping and crossover to Drude metallic behavior at large doping resembles that is seen in borophene without polar substrate. We exercise caution in interpreting the origin of low peak resonance in the Lorenz ratio since such anomaly arises not only from electronic mechanism but also via electron-phonon coupling.

We elaborate the analysis of charge and heat transport by looking the impact by nonequilibrium phonon, which is responsible for the phonon drag effect. By concentrating on the acoustic phonon, we have analyzed drag thermopower at low temperature, i.e., $T < 50$ K by employing RTA with the aim of deriving an analytical solution of the drag coefficient. At low temperature, without the tilted velocity, we derived an analytical expression of the drag thermopower showing a T^3 power law similar to that known for graphene. The drag thermopower of borophene is, however, different from that graphene in a way that its magnitude varies according to the axes, i.e., thermopower on the x falls lower than that on the y axis, which tends to become more visible at higher temperature. We argue that this unique drag property of borophene might be used as hint for phonon drag effect in the thermopower since its detection based on the variation of magnitude remains inconclusive.

Another important aspect of transport discussed in this paper is the cooling mechanism, a transfer of energy between borophene with phonon. By means of RTA, we first demonstrate that in the absence of tilted velocity, a power loss of borophene with acoustic phonon takes a similar process to that of graphene. On the other hand for nonzero tilted

velocity, power loss slightly decreases and such behavior is further evident with the increase of doping. While a similar is also seen when polar substrate is employed, we also find that the exchange energy becomes larger than that with acoustic phonon signifying the possibility of rapid cooling mechanism.

The question of whether monolayer borophene either suspended or supported could become a promising material for thermoelectric application, has also been addressed in this paper. Our discussion without including phonon shows that borophene achieves a figure of merit (FOM) nearly to one, which is comparable to that graphene and many thermoelectric materials currently employed as thermoelectric material. A rather similar result is also seen in the case of supported borophene by taking effect of both impurity and acoustic phonon. We discuss the possibility of enhancing figure of merit by inducing defects, i.e., adding an impurity concentration. Our result shows that such effort indeed slightly increases FOM and might be a viable choice whenever the impact of electron-phonon coupling becomes increasingly important in the supported borophene.

In the present paper, we have also demonstrated that relaxation time approximation, which abandons variation of angle of Fermi wave vectors still captures some essential ingredients of transport. This is true in the case of borophene with anisotropic Fermi surface despite having sacrificed contribution of scattering beyond circular Fermi surface, which eventually results in a loss of accuracy. The iterative solution of Boltzmann transport yields qualitative and quantitative improvement, which is expected to approach an exact solution. Its additional advantage is the consistency of observables whenever the anisotropy of the mean-free path or relaxation time becomes crucial such as shown above in the analysis of the Lorenz ratio.

-
- [1] X. Wu, J. Dai, Y. Zhao, Z. Zho, J. Yang, and X. C. Zeng, Two-dimensional boron monolayer sheets, *ACS Nano* **6**, 7443 (2012).
- [2] A. J. Mannix, X.-F. Zhou, B. Kiraly, J. D. Wood, D. Alducin, B. D. Myers, X. Liu, B. L. Fisher, U. Santiago, J. R. Guest *et al.*, Synthesis of borophenes: Anisotropic, two-dimensional boron polymorphs, *Science* **350**, 1513 (2015).
- [3] B. Feng, J. Zhang, Q. Zhong, W. Li, S. Li, H. Li, P. Cheng, S. Meng, L. Chen, and K. Wu, Experimental realization of two-dimensional boron sheets, *Nat. Chem.* **8**, 563 (2016).
- [4] B. Feng, J. Zhang, R.-Y. Liu, T. Iimori, C. Lian, H. Li, L. Chen, K. Wu, S. Meng, F. Komori, and I. Matsuda, Direct evidence of metallic bands in a monolayer boron sheet, *Phys. Rev. B* **94**, 041408(R) (2016).
- [5] E. D. Sandoval, S. Hajinazar, and A. N. Kolmogorov, Stability of two-dimensional BN-Si structures, *Phys. Rev. B* **94**, 094105 (2016).
- [6] S.-G. Xu, X.-T. Li, Y.-J. Zhao, J.-H. Liao, W.-P. Xu, X.-B. Yang, and H. Xu, Two-dimensional semiconducting boron monolayers, *J. Am. Chem. Soc.* **139**, 17233 (2017).
- [7] W. W. Luo, G. Liu, X. Wang, X. L. Lei, C. Y. Ouyang, and S. Q. Liu, The adsorption and dissociation of oxygen on Ag (111) supported χ_3 borophene, *Phys. B: Condens. Matter* **537**, 1 (2018).
- [8] A. Ahmadi, M. Masoudi, N. Taghizadeh, H. Jafaric, and M. Faghinihasiri, Study of mechanical and electronic properties of single-layer FeB₂, *Phys. E* **112**, 71 (2019).
- [9] R. Wu, I. K. Drozdov, S. Eltinge, P. Zahl, S. Ismail-Beigi, I. Božović, and A. Gozar, Large-area single-crystal sheets of borophene on Cu(111) surfaces, *Nat. Nano.* **14**, 44 (2019).
- [10] F. Ma, Y. Jiao, G. Gao, Y. Gu, A. Bilic, Z. Chen, and A. Du, Graphene-like two-dimensional ionic boron with double Dirac cones at ambient condition, *Nano Lett.* **16**, 3022 (2016).
- [11] A. Lopez-Bezanilla and P. B. Littlewood, Electronic properties of 8-*Pmmn* borophene, *Phys. Rev. B* **93**, 241405(R) (2016).
- [12] M. Nakhaee, S. A. Ketabi, and F. M. Peeters, Tight-binding model for borophene and borophane, *Phys. Rev. B* **97**, 125424 (2018).
- [13] P. Ranjan, T. K. Sahu, R. Bhushan, S. Yamijala, D. J. Late, P. Kumar, and A. Vinu, Freestanding borophene and its hybrids, *Adv. Mater.* **31**, 1900353 (2019).
- [14] A. A. Balandin, S. Ghosh, W. Bao, I. Calizo, D. Teweldebrhan, F. Miao, and C. N. Lau, Superior thermal conductivity of single-layer graphene, *Nano Lett.* **8**, 902 (2008).

- [15] K. I. Bolotina, K. J. Sikes, Z. Jianga, M. Klimac, G. Fudenberga, J. Honec, P. Kima, and H. L. Stormer, Ultrahigh electron mobility in suspended graphene, *Solid State Commun.* **146**, 351 (2008).
- [16] S. Chen, A. L. Moore, W. Cai, J. W. Suk, J. An, C. Mishra, C. Amos, C. W. Magnuson, J. Kang, L. Shi, and R. S. Ruoff, Raman measurements of thermal transport in suspended monolayer graphene of variable sizes in vacuum and gaseous environments, *ACS Nano* **5**, 321 (2011).
- [17] Y.-W. Tan, Y. Zhang, K. Bolotin, Y. Zhao, S. Adam, E. H. Hwang, S. Das Sarma, H. L. Stormer, and P. Kim, Measurement of Scattering Rate and Minimum Conductivity in Graphene, *Phys. Rev. Lett.* **99**, 246803 (2007).
- [18] X. Hong, K. Zou, and J. Zhu, Quantum scattering time and its implications on scattering sources in graphene, *Phys. Rev. B* **80**, 241415(R) (2009).
- [19] C. Berger, Z. Song, X. Li, X. Wu, N. Brown, C. Naud, D. Mayou, T. Li, J. Hass, A. N. Marchenkov *et al.*, Electronic confinement and coherence in patterned epitaxial graphene, *Science* **312**, 1191 (2006).
- [20] J. A. Robinson, M. Wetherington, J. L. Tedesco, P. M. Campbell, X. Weng, J. Stitt, M. A. Fanton, E. Frantz, D. Snyder, B. L. VanMil *et al.*, Correlating raman spectral signatures with carrier mobility in epitaxial graphene: A guide to achieving high mobility on the wafer scale, *Nano Lett.* **9**, 2873 (2009).
- [21] C. R. Dean, A. F. Young, I. Meric, C. Lee, L. Wang, S. Sorgenfrei, K. Watanabe, T. Taniguchi, P. Kim, K. L. Shepard, and J. Hone, Boron nitride substrates for high-quality graphene electronics, *Nat. Nano* **5**, 722 (2010).
- [22] J. Yuan, N. Yu, K. Xue, and X. Miao, Ideal strength and elastic instability in single-layer 8-*Pmmn* borophene, *RSC Adv.* **7**, 8654 (2017).
- [23] A. D. Zabolotskiy and Y. E. Lozovik, Strain-induced pseudo-magnetic field in the dirac semimetal borophene, *Phys. Rev. B* **94**, 165403 (2016).
- [24] S. K. Firoz Islam and A. M. Jayannavar, Signature of tilted Dirac cones in Weiss oscillations of 8-*Pmmn* borophene, *Phys. Rev. B* **96**, 235405 (2017).
- [25] S. Verma, A. Mawrie, and T. K. Ghosh, Effect of electron-hole asymmetry on optical conductivity in 8-*Pmmn* borophene, *Phys. Rev. B* **96**, 155418 (2017).
- [26] S.-H. Zhang and W. Yang, Oblique Klein tunneling in 8-*Pmmn* borophene p-n junctions, *Phys. Rev. B* **97**, 235440 (2018).
- [27] P. Sengupta, Y. Tan, E. Belotti, and J. Shi, Anomalous heat flow in 8-*Pmmn* borophene with tilted Dirac cones, *J. Phys.: Condens. Matter* **30**, 435701 (2018).
- [28] A. E. Champo and G. G. Naumis, Metal-insulator transition in 8-*Pmmn* borophene under normal incidence of electromagnetic radiation, *Phys. Rev. B* **99**, 035415 (2019).
- [29] B. D. Napitu, Photoinduced Hall effect and transport properties of irradiated 8-*Pmmn* borophene monolayer, *J. Appl. Phys.* **127**, 034303 (2020).
- [30] X. Zhou, Anomalous Andreev reflection in an 8-*Pmmn* borophene-based superconducting junction, *Phys. Rev. B* **102**, 045132 (2020).
- [31] T. Cheng, H. Lang, Z. Li, Z. Liu, and Z. Liu, Anisotropic carrier mobility in two-dimensional materials with tilted Dirac cones: Theory and application, *Phys. Chem. Chem. Phys.* **19**, 23942 (2017).
- [32] M. Zare, Thermoelectric transport properties of borophane, *Phys. Rev. B* **99**, 235413 (2019).
- [33] K. Výborný, A. A. Kovalev, J. Sinova, and T. Jungwirth, Semiclassical framework for the calculation of transport anisotropies, *Phys. Rev. B* **79**, 045427 (2009).
- [34] T. Stauber, N. M. R. Peres, and F. Guinea, Electronic transport in graphene: A semiclassical approach including midgap states, *Phys. Rev. B* **76**, 205423 (2007).
- [35] A. Rycerz, Wiedemann-Franz law for massless Dirac fermions with implications for graphene, *Materials* **14**, 2704 (2021).
- [36] D. A. Bandurin, I. Torre, R. K. Kumar, M. B. Shalom, A. Tomadin, A. Principi, G. H. Auton, E. Khestanova, K. S. Novoselov, I. V. Grigorieva *et al.*, Negative local resistance caused by viscous electron backflow in graphene, *Science* **351**, 1055 (2016).
- [37] J. Crossno, J. K. Shi, K. Wang, X. Liu, A. Harzheim, A. Lucas, S. Sachdev, P. Kim, T. Taniguchi, K. Watanabe, T. A. Ohki, and K. C. Fong, Observation of the Dirac fluid and the breakdown of the Wiedemann-Franz law in graphene, *Science* **351**, 1058 (2016).
- [38] E. H. Hwang and S. Das Sarma, Acoustic phonon scattering limited carrier mobility in two-dimensional extrinsic graphene, *Phys. Rev. B* **77**, 115449 (2008).
- [39] S. Yiğen, V. Tayari, J. O. Island, J. M. Porter, and A. R. Champagne, Electronic thermal conductivity measurements in intrinsic graphene, *Phys. Rev. B* **87**, 241411(R) (2013).
- [40] J. Y. Kim, C. Lee, S. Bae, K. S. Kim, B. H. Hong, and E. J. Choi, Far-infrared study of substrate-effect on large scale graphene, *Appl. Phys. Lett.* **98**, 201907 (2011).
- [41] V. Perebeinos and P. Avouris, Inelastic scattering and current saturation in graphene, *Phys. Rev. B* **81**, 195442 (2010).
- [42] A. Konar, T. Fang, and D. Jena, Effect of high- κ gate dielectrics on charge transport in graphene-based field effect transistors, *Phys. Rev. B* **82**, 115452 (2010).
- [43] D. G. Cantrell and P. N. Butcher, A calculation of the phonon-drag contribution to the thermopower of quasi-2D electrons coupled to 3D phonons: I. General theory, *J. Phys. C* **20**, 1985 (1987).
- [44] D. G. Cantrell and P. N. Butcher, A calculation of the phonon-drag contribution to the thermopower of quasi-2D electrons coupled to 3D phonons. II. Applications, *J. Phys. C* **20**, 1993 (1987).
- [45] A. C. Betz, F. Violla, D. Brunel, C. Voisin, M. Picher, A. Cavanna, A. Madouri, G. Fève, J.-M. Berroir, B. Plaçais, and E. Pallicchi, Hot Electron Cooling by Acoustic Phonons in Graphene, *Phys. Rev. Lett.* **109**, 056805 (2012).
- [46] C. B. M. D. E. Prober and B. S. Karasik, Performance of graphene thermal photon detectors, *J. Appl. Phys.* **113**, 044512 (2013).
- [47] S. S. Kubakaddi, Interaction of massless Dirac electrons with acoustic phonons in graphene at low temperatures, *Phys. Rev. B* **79**, 075417 (2009).
- [48] X. Li, E. A. Barry, J. M. Zavada, M. B. Nardelli, and K. W. Kim, Surface polar phonon dominated electron transport in graphene, *Appl. Phys. Lett.* **97**, 232105 (2010).